Composite Analysis of Winter Cyclones in a GCM: Influence on Climatological Humidity

MIKE BAUER

Department of Earth and Environmental Sciences, Columbia University, New York, New York

ANTHONY D. DEL GENIO

NASA Goddard Institute for Space Studies, New York, New York

(Manuscript received 22 January 2005, in final form 20 July 2005)

ABSTRACT

The role of midlatitude baroclinic cyclones in maintaining the extratropical winter distribution of water vapor in an operational global climate model is investigated. A cyclone identification and tracking algorithm is used to compare the frequency of occurrence, propagation characteristics, and composite structure of 10 winters of storms in the Goddard Institute for Space Studies general circulation model (GCM) and in two reanalysis products. Cyclones are the major dynamical source of water vapor over the extratropical oceans in the reanalyses. The GCM produces fewer, generally weaker, and slower-moving cyclones than the reanalyses and is especially deficient in storms associated with secondary cyclogenesis. Composite fields show that GCM cyclones are shallower and drier aloft than those in the reanalyses and that their vertical structure is less tilted in the frontal region because of the GCM's weaker ageostrophic circulation. This is consistent with the GCM's underprediction of midlatitude cirrus. The GCM deficiencies do not appear to be primarily due to parameterization errors; the model is too dry despite producing less storm precipitation than is present in the reanalyses and in an experimental satellite precipitation dataset, and the weakness and shallow structure of GCM cyclones is already present at storm onset. These shortcomings may be common to most climate GCMs that do not resolve the mesoscale structure of frontal zones, and this may account for some universal problems in climate GCM midlatitude cloud properties.

1. Introduction

Baroclinic cyclones are an ever present and conspicuous form of extratropical weather. Cyclone activity strongly influences the extratropical distribution of cloud, precipitation, and water vapor. As the primary agents of poleward heat and moisture transport, cyclones balance the planetary budgets of energy and water. Therefore, the ability to simulate cyclones is a fundamental test for any global climate model.

In principle, climate models benefit from decades of research in numerical weather prediction (NWP) and should be able to simulate the water vapor, cloud, and precipitation fields associated with cyclones with some fidelity. In practice, however, NWP models resolve the mesoscales at which frontogenesis occurs, while global climate models currently do not, and NWP model validation focuses on reducing short-term forecast errors, whereas climate model validation has emphasized statistical standards such as climatological mean fields.

Traditional climate model validation techniques risk climatological correctness in the face of meteorological inaccuracy. We instead pursue a process-based approach to validating the water vapor distribution in a general circulation model/global climate model (GCM) by examining the composite structure of dynamical and humidity fields around baroclinic cyclones. Compositing has frequently been used to examine dynamical processes such as explosive cyclogenesis (Manobianco 1989) and wave packet development (Hakim 2003). For our purposes, composite analysis renders a representative picture of cyclone effects on water vapor from all the inherent case-to-case variability in a way that points to specific model deficiencies.

The distribution of water vapor around a cyclone

Corresponding author address: Dr. Anthony D. Del Genio, NASA Goddard Institute for Space Studies, 2880 Broadway, New York, NY 10025.
E-mail: adelgenio@giss.nasa.gov

closely reflects the organized circulation pattern necessary for a baroclinic system to exist and grow. Observation-based composite studies reveal distinct patterns in the distribution of water vapor, surface latent heat flux, cloud, and precipitation near cyclones (McMurdie and Katsaros 1985; Miller and Katsaros 1992; Lau and Crane 1995; Petty and Miller 1995; Miller and Petty 1998; Klein and Jakob 1999). Distinct differences exist in these patterns as a function of life cycle stage, strength, and deepening rate, because humidity strongly depends on the cyclone's velocity field (Holton 1992; Carlson 1998). This dynamical constraint is so strong that reanalysis forecasts done with and without humidity observations give nearly identical results (Bengtsson et al. 2004). Thus, the reanalysis water vapor fields themselves must be evaluated against available data.

Observed extratropical water vapor transports primarily occur as high-intensity filamentary plumes of warm, moist air known as tropospheric rivers or warm conveyor belts (Zhu and Newell 1998; Eckhardt et al. 2004; Ralph et al. 2004). Rivers often associate with and amplify extratropical cyclones, flowing along the leading edge of the surface cold front before rapidly ascending just to the east of the surface low (Carlson 1998; Browning 1999). They are the main ascending branch in a baroclinic cyclone as well as a primary pathway for boundary layer air to reach the midlatitude upper troposphere (Cotton et al. 1995; Cooper et al. 2001; Stohl 2001; Eckhardt et al. 2004). In this role, warm conveyor belts carry about one-third of the total upward mass flux around a typical cyclone and create about as much of its lifetime precipitation (Eckhardt et al. 2004). Cyclones containing warm conveyor belts (~60% of the total) produce about twice as much precipitation as do similar cyclones that lack a warm conveyor belt. As a result, warm conveyor belts deposit ~40%–70% of the precipitation in the wintertime storm tracks. Given the coarse dynamic grid of climate GCMs, there is ample reason to wonder if these models can adequately resolve such subcyclone-scale water vapor transports.

Further motivation for this study comes from the desire to understand the apparent dry and cool bias of the Goddard Institute for Space Studies (GISS) GCM's wintertime extratropical upper troposphere. The GCM is ~1% drier in midlatitudes than the Television Infrared Observation Satellite (TIROS) Operational Vertical Sounder (TOVS)/High Resolution Infrared Radiation Sounder (HIRS) estimate (Bates et al. 2001), which is itself dry biased (Lanzante and Gahrs 2000), with an even larger bias in the East Asian storm-track region. Furthermore, the GCM underestimates midlatitude clear-sky aerosol optical depths and underpredicts extratropical high-cloud cover (Del Genio et al. 1996; Tselioudis and Jakob 2002; Schmidt et al. 2006).

The distribution of cloud, like water vapor, depends heavily on the motions associated with cyclones (Wang and Fu 2000a). Reanalyses successfully reproduce the general properties of the observed cyclone–cloud distribution (Klein and Jakob 1999; Tselioudis and Jakob 2002). Even so, reanalysis low cloud is too sparse and close to the surface in regions of descending cyclone motion, and cyclone clouds tend to be too optically thick, especially in ascending regions (Tselioudis and Jakob 2002). Peak high-cloud amounts also coincide more closely with peak ascent than observations suggest (Klein and Jakob 1999).

Tselioudis and Jakob (2002) examined cyclone-related cloud in the GISS GCM as well. In general, the GCM and reanalysis clouds are quite similar and even share many shortcomings. On the other hand, cyclones in the GCM are relatively lacking in high cloud wherever upward motion exists, consistent with the GCM's high-cloud deficiency over the Northern Hemisphere wintertime storm tracks (Del Genio et al. 1996). Tselioudis and Jakob (2002) further suggest that because this cloud deficiency occurs only under very specific conditions, it is unlikely to be a cloud parameterization issue. We suggest in this paper that this problem is the direct result of the GISS GCM's cyclones being comparatively shallow, slow moving, and dry aloft (due to ascending motion that is too weak and too upright) for a given surface intensity.

In what follows, we use the GISS GCM, reanalyses, and observations to explore these issues. In section 2 we describe the models and datasets being used, our approach to cyclone tracking and compositing, and our definition of cyclone intensity. In section 3, we compare observed water vapor climatologies with those from the reanalyses and the GCM. Section 4 details the spatial, temporal, and intensity distribution of cyclones in the GCM and reanalysis products. In section 5 we analyze GCM and reanalysis storm composite dynamical fields, humidity, and precipitation. In section 6 we discuss the implications of our findings for climate model development and interpretation.

2. Methods

a. Model and data

We use GISS GCM version Model E 2.3.4 (Schmidt et al. 2006) at $4° \times 5° \times 23$ layer resolution. The model includes a new atmospheric-turbulence parameterization (which produces more realistic water vapor transport out of the boundary layer), improved water vapor advection near steep topography, and updates to con-

vective and stratiform precipitation microphysics. We base our analysis on 3-hourly samples from 10 Northern Hemisphere winters [December–January–February (DJF)] extracted from a longer control run with climatological sea surface temperatures, sea ice, and atmospheric composition. Despite its coarse resolution, this model is of general relevance because (a) it is used for GISS Intergovernmental Panel on Climate Change Fourth Assessment Report simulations (cf. Hansen et al. 2005), and (b) midlatitude cloud property errors in this GCM are similar to those in higher-resolution climate GCMs (Zhang et al. 2005).

For comparison, we use a 10-winter subset (December 1979–February 1989) from the 40-yr European Centre for Medium-Range Weather Forecasts Re-Analysis (ERA-40; Simmons and Gibson 2000). ERA-40 products are available as 6-hourly samples on a 2.5° × 2.5° grid created from a forecast at T159 spectral resolution (about a 1.125° × 1.125° grid) with 60 sigma levels. We also examine products for the same time period and at similar resolution from the National Centers for Environmental Prediction–National Center for Atmospheric Research (NCEP–NCAR) reanalysis (NRA; Kalnay et al. 1996; Kistler et al. 2001). Trends in storm activity were not removed from the reanalyses but are fairly small over the 10-yr period we analyze (Chang and Fu 2002).

As mentioned earlier, reanalysis water vapor fields are influenced more by the underlying dynamics than by ingested water vapor observations. Thus, it would be preferable to analyze humidity observations. Unfortunately, long-term global water vapor datasets are unavailable on the subdaily time scales required for composite analysis. Thus, we are limited to using these observations to judge the large-scale time-average conditions in the GCM and reanalyses. For upper-troposphere relative humidity (UTH) we use TOVS/HIRS 6.7-μm retrievals (Bates et al. 2001), which represent a broad layer centered on ~300 hPa. The data are available as monthly means for latitudes below 60° over the period 1980–89. TOVS/HIRS retrievals are unreliable when thick cloud is present (Soden and Bretherton 1993). Cloud clearing, however, introduces a sampling bias toward clear-sky conditions (i.e., for noncyclone conditions), which creates a climatological dry bias in the extratropics of a few percent relative humidity (Lanzante and Gahrs 2000). We use the National Aeronautics and Space Administration (NASA) Water Vapor Project dataset (NVAP) for the climatology of lower-tropospheric water vapor (Randel et al. 1996). NVAP is a blended, global, daily analysis of water vapor from radiosondes, TOVS, and passive microwave data, available as monthly means for 1988–99. A main limitation of this product is that the data sources vary with time, place, and condition, owing to issues of data availability, quality, and appropriateness.

Precipitation is an important sink for water vapor in midlatitude cyclones. Huffman et al. (2003) have produced an experimental 3-hourly real-time satellite precipitation analysis by applying combined microwave-infrared retrievals developed for the Tropical Rainfall Measuring Mission (TRMM) to data from all available satellites. These data are available for the period 2001–04 and their temporal resolution allows us to produce 6-hourly accumulation storm precipitation composites. Solid precipitation, precipitation over land, and light rain are underestimated in these retrievals, so to minimize these biases, we restrict our analysis to latitudes below 50° and also mask land areas and areas with composite rainfall <1 mm day^{-1} in both the data and the models.

b. Automated cyclone identification and tracking

Extratropical cyclones are conveniently understood by the Norwegian–Bjerknes archetype of a coherent and mobile atmospheric circulation focused around a low pressure center, but observed cyclones inevitably differ in some way from this model. This creates a problem of finding a method of cyclone identification that is flexible enough to capture most cyclones and yet selective enough to exclude noncyclone disturbances. Cyclone identification strongly depends on the meteorological variable being searched (e.g., sea level pressure or vorticity), and on the sampling properties of a given dataset (Sinclair 1994). These compounding sensitivities make composite analysis somewhat contingent upon the method being used (Gulev et al. 2001; Paciorek et al. 2002).

We opt for the traditional and favored method of locating and tracking sea level pressure (SLP) minima, using a cyclone-tracking algorithm much like that of Chandler and Jonas (1999). SLP-based tracking algorithms are biased toward well-developed and relatively slow-moving systems (Sinclair 1994, 1997), which GCMs have some difficulty generating (Lambert et al. 2002). SLP tracking has difficulty seeing the poorly defined SLP fields associated with early and late-stage cyclones and thus underestimates cyclone duration and extent (Sinclair 1994; Gulev et al. 2001). It also neglects fast-moving open-wave systems that overrun stationary lows or pass through the strong background pressure gradients associated with enhanced westerly winds (Sinclair 1994; Blender and Schubert 2000; Gulev et al. 2001). These open-wave systems can nonetheless have

comma cloud structures, well-developed cyclonic circulations, and strong precipitation bands (Sinclair 1997). On the other hand, SLP-based tracking sidesteps the inherent resolution dependence of the main alternative technique, which tracks geostrophic vorticity maxima. This is not an issue for observational studies (cf. Hakim 2003) but is an important consideration for us given the different resolution of the GCM and reanalyses we wish to compare. Furthermore, inspection of individual storms suggests that the tropospheric rivers that are important to heat and water vapor transport tend to accompany cyclones of the sort that SLP tracking is adept at detecting, whereas the fast-moving open systems that SLP tracking often overlooks, although common, may not be particularly important to water vapor transport.

The first step of our algorithm screens the SLP field for local (within a 3×3 grid box area) minima, that is, closed isobar features, of which ~600 000 exist for the 10 Northern Hemisphere winters in the GCM. The next step pairs candidate minima with others from the preceding time step, assuming that storms cannot propagate more than 720 km over this time (i.e., at speeds >120 km h^{-1}). If a local low falls within the 720-km search radius of a low from a preceding time step, it is assumed to be a continuation of the previous cyclone; if not, it is categorized as a new cyclone. Successful matches are then joined into a track representing the sequential path of a potential cyclone. When multiple SLP minima are found within the search radius at a given time, only the deepest is retained; this eliminates some secondary cyclones but reduces ambiguity in defining tracks. Tracking includes information from November and March to ensure that any DJF cyclone is completely represented. About one-third of all minima can be placed into such tracks.

We then apply three additional screening criteria to isolate cyclones. First, cyclones must last at least 24 h. Second, cyclones must attain a lifetime minimum SLP of at least 1010 hPa. Third, cyclones must travel at least 700 km in latitude and longitude; this helps eliminate spurious lows at high elevations. In addition, we split cyclone tracks that make a greater-than-right-angled relative course change persisting at least 24 h. This step serves to capture secondary redevelopment or wake cyclogenesis as separate systems rather than as a continuation of the primary one. Fewer than 1% of the candidate SLP minima meet all selection criteria.

Our selection criteria are similar to those used in previous studies (König et al. 1993; Sinclair 1994; Blender et al. 1997; Zhang and Wang 1997; Blender and Schubert 2000; Gulev et al. 2001; Paciorek et al. 2002). Aside from the requirement to filter out stationary lows, the criteria are quasi redundant, that is, suppressing one simply evokes another more often, resulting in only modest changes in the database. For example, suppressing the minimum lifetime criterion increases the number of storms by 21%, almost all of them weak, while eliminating the minimum SLP magnitude criterion has no net effect. Radically changing the criteria primarily allows two unwanted types of systems into our database: purely tropical systems and spurious events associated with inaccurate sea level pressure reduction over high terrain (e.g., Greenland and the Tibetan Plateau).

c. *Compositing and intensity measures*

We next sort the storm database by intensity, based on the observation that stronger storms have stronger winds, sharper thermal/moisture contrasts, elevated surface evaporation, more vigorous vertical motions, and more condensation/precipitation (Miller and Katsaros 1992; Petty and Miller 1995; Miller and Petty 1998). We follow the multivariate approach of Zielinski (2002). By combining three commonly used measures of cyclone intensity (minimum lifetime SLP, deepening rate, and pressure gradient) into a single index, this method hopes to overcome some of the known shortcomings of using these measures individually (Sinclair 1997; Sinclair and Revell 2000; Paciorek et al. 2002). Our intensity index (units of hPa) can be written as

$$I = (1013 - \text{SLP}) + \text{deepening change} + \text{pressure contrast}.$$

The deepening change (24-h decrease of central SLP) is taken over the 24 h preceding the SLP minimum. A few cyclones are first detected at or near their minimum lifetime SLP (due to the breakup of a preexisting system). In these cases, the SLP tendency of the succeeding 24 h is used instead. The pressure contrast (change of SLP over 1000 km) is the maximum value within a 1500-km radius of the SLP minimum. Results using only the first term in the equation for I mainly affect continental storms and have little effect on Northern Hemisphere ocean cyclones.

We divide the resulting distribution of intensities by quartiles, with the most (least) intense 25% of all cyclones being designated as "strong" ("weak"). "Intermediate" cyclones occupy the middle 50% of the distribution. This gives threshold values between classes similar to those used by Zielinski (2002) based on historical accounts of storm damage, although these values differ somewhat between the GCM and the reanalyses. As a result, we use the ERA-40 thresholds as the common intensity scale to sort each database. The ERA-40

has ~5% more maritime cyclones than does the NRA (most of these in the strong category). Primarily this is the result of slight placement differences of some coastal cyclones. The remaining difference is related to artifacts of sea level pressure reduction over high coastal terrain or because our tracking scheme splits ERA-40 cyclones more often than NRA cyclones. For maximum interoperability then, we use our ERA-40 cyclone database whenever compositing NRA products, that is, our ERA-40 and NRA composites are for exactly the same systems.

Composite fields for each intensity class are then produced by averaging the fields for all cyclones on a common grid spanning ~±25° in latitude and longitude (13 × 11 grid boxes for the GCM, 21 × 21 for the reanalyses) and whose origin is centered on the location of each storm's lifetime SLP minimum. GCM fields are instantaneously interpolated from model sigma levels to standard reanalysis pressure levels for comparison. Compositing works best when the cyclones are as similar as possible to begin with (Sinclair and Revell 2000). Most cyclones in our database (~71%, and nearly all strong ones) reach peak intensity over ocean, consistent with observations (Sanders and Gyakum 1980; Roebber 1984; Paciorek et al. 2002). Maritime systems in our database are warmer and more humid than continental systems of the same intensity and are less variable from one system to another. In addition, most meridional and vertical water vapor transports occur over ocean in association with tropospheric rivers and maritime cyclones. For simplicity, we therefore exclude the complicating influences of cyclones that peak over land altogether. We further exclude systems that never leave the Tropics (i.e., those equatorward of 30°) or those that always remain poleward of the Arctic Circle.

Some complications are more difficult to resolve through such simplifications (cf. Gyakum et al. 1989; Lambert 1996). For example, most intense cyclones peak near the Aleutian and Icelandic lows. Thus, strong cyclone composites represent higher (colder) latitudes than do weak cyclone composites. Also, strong cyclones with large deepening rates are longer lived than similarly intense cyclones that deepen more slowly. Thus, cyclones from the same category may reach peak intensity at different latitudes given the same origins. We have not made geostrophic adjustments for cyclones from different latitudes (cf. Sanders and Gyakum 1980), which slightly blurs the distinction between intensity classes. However, this should have little effect on our comparisons, since mean GCM and reanalysis cyclone locations differ only by a degree or two, and strong cyclones peak only ~3° poleward of weak cyclones on average.

3. Climatological humidity fields

Figure 1 compares the winter water vapor climatologies in the two reanalyses to the TOVS/HIRS and NVAP retrievals, while Table 1 summarizes the hemispheric mean differences. The TOVS/HIRS retrieval uses infrared emission by water vapor to infer UTH. In thick cloud-covered regions, emission is primarily from cloud top and a UTH retrieval is not performed. This creates a bias toward clear-sky conditions, which are drier on average. Lanzante and Gahrs (2000) estimate a global bias of a few percent based on comparisons to soundings from 63 upper-air stations. The NVAP retrieval combines data from three sources (radiosondes, TOVS, and microwave) with complementary sampling characteristics. Column water vapor is moist biased over desert regions, where microwave retrievals are not performed and radiosonde coverage is sparse (Randel et al. 1996). Over ocean, NVAP is globally dry biased by ~1 mm relative to an independent ground-validated satellite microwave retrieval; in midlatitudes the dry bias is greatest over the storm tracks, while the eastern oceans are moist biased (Simpson et al. 2001).

ERA-40 UTH is within ~10% of the TOVS retrieval everywhere except for a modest dry bias along the East Asian seaboard; most of the 5.9% hemispheric mean difference can probably be attributed to the slight dry bias of TOVS. NRA, on the other hand, is considerably (>20%) wetter than TOVS, particularly over the central and eastern oceans. Examination of several individual storms suggests that the NRA moist bias may in part be related to tropical and subtropical excess moisture that is subsequently transported to midlatitudes (Bauer 2005). Total column water vapor fields (dominated by lower-troposphere humidity) are fairly similar in the two reanalyses, both showing moist biases over the eastern Atlantic and subtropical east Pacific Oceans and dry biases along the Asian and North American cyclogenesis and storm-track regions. ERA-40 is too moist south of the Pacific storm track, and NRA is moist biased over the northeast Pacific. Overall, NRA regional column water vapor biases are slightly smaller than those of ERA-40. Taken together, we conclude that ERA-40 is the better choice for constructing three-dimensional cyclone composite humidity fields for comparison to the GCM.

This conclusion, however, assumes that cyclones are important contributors to the climatological extratropical humidity. To demonstrate that this is the case, we partition the time history of the ERA-40 humidity field into a part associated with cyclones (encompassing ±25° latitude–longitude from the surface pressure minima in our database) and another residual part that

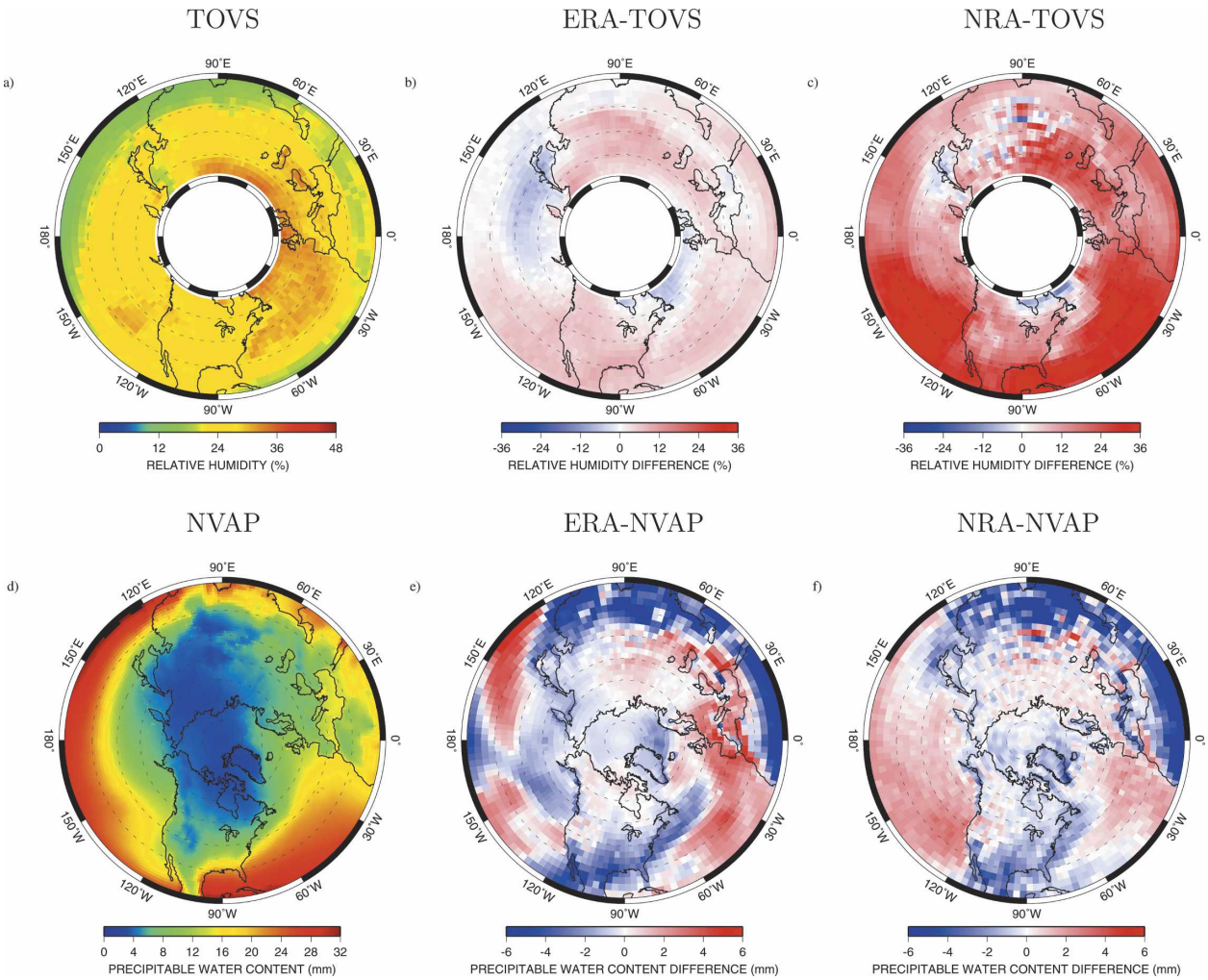

FIG. 1. (top) Time-average DJF UTH (%) distribution for 20°–90°N: (a) TOVS/HIRS, (b) ERA-40–TOVS difference, and (c) NRA–TOVS difference. (bottom) Same as in top, but for (d) NVAP total column water vapor (mm), (e) ERA-40–NVAP difference, and (f) NRA–NVAP difference. TOVS UTH humidities are expressed with respect to ice saturation but were converted to estimated humidities with respect to water saturation for the purposes of this figure using NRA temperature fields.

is not. Figure 2 shows the time-average contributions made by each part to the total, that is, $RH = a \times RH_{cyclone} + (1 - a) \times RH_{other}$, where a is the frequency of occurrence of cyclones. Cyclones contribute most of the water vapor over midlatitude oceans, especially over the Pacific and Atlantic storm tracks, and along the east coasts of Asia and North America. Peak upward motion and relative humidity typically occur south and east of the cyclone center, and so the peak cyclone contributions (especially in the upper tropo-

TABLE 1. Differences between DJF average reanalysis humidities and observations. (top) The 300-hPa relative humidity, 20°–60°N (%), (middle) the 850-hPa relative humidity, 20°–90°N (%), (bottom) total column water vapor (TCWV), 20°–90°N (mm). The first column lists observations and the next three list ERA-40–observation, NRA–observation, and ERA-40–NRA differences expressed as mean and (in parentheses) rms errors.

	Obs	ERA-40–Obs	NRA–Obs	ERA-40–NRA
300 hPa	25.1%	5.9 (7.3)%	21.5 (24.1)%	−15.6 (18.2)%
850 hPa	—	—	—	9.2 (14.2)%
TCWV	8.44 mm	−0.38 (1.83) mm	−0.36 (1.67) mm	−0.02 (1.33) mm

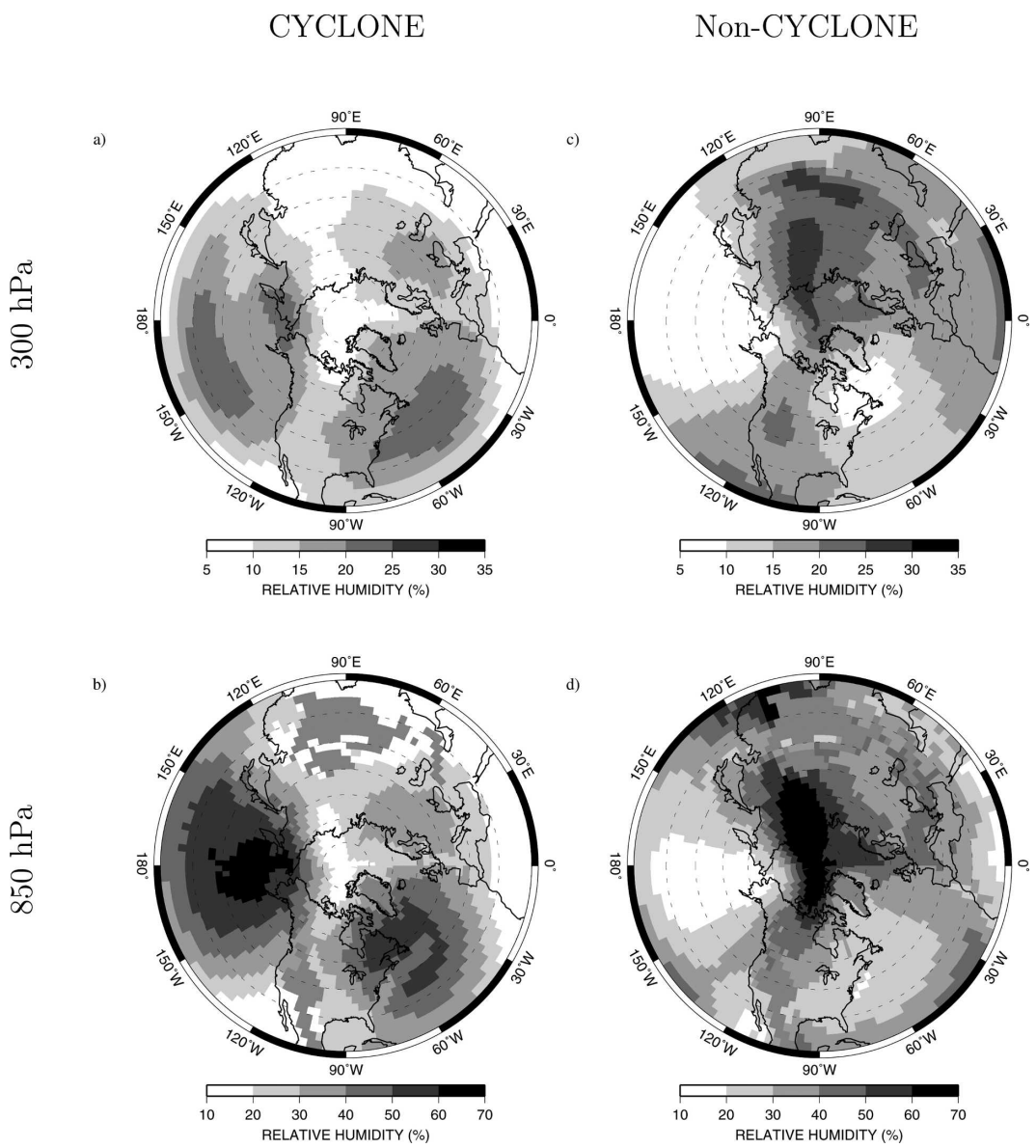

FIG. 2. ERA-40 (a), (c) 300- and (b), (d) 850-hPa climatological relative humidities separated into cyclone-connected and residual contributions. When added, the left and right panels equal the mean humidity fields at each level.

sphere) are somewhat displaced from the center of the storm tracks themselves. The NRA exhibits similar patterns but is more exaggerated in the upper troposphere (Bauer 2005), suggesting that its wet upper-level bias is associated with cyclone processes. Noncyclone sources regulate humidity in other regions. For example, tropical and subtropical tropospheric rivers that are not related to cyclones make significant contributions to extratropical humidity in the eastern ocean basins and to a lesser extent at higher latitudes along the west coasts of North America and Europe.

Figure 3 compares the upper- and lower-troposphere humidity fields of the GCM to those of ERA-40. In the upper troposphere, the GCM is generally too moist at low latitudes and too dry over high-latitude continents and the Arctic Basin, but its mean relative humidity field is generally good over the extratropical oceans. As we will see later, the GCM nonetheless underestimates specific humidity in the storm tracks because of a cold bias there and has a narrower distribution of humidity values in storm regions than the reanalysis. Over East Asia, the GCM is somewhat too dry even in relative humidity. In the lower troposphere, generally similar GCM–reanalysis differences exist, with the exception

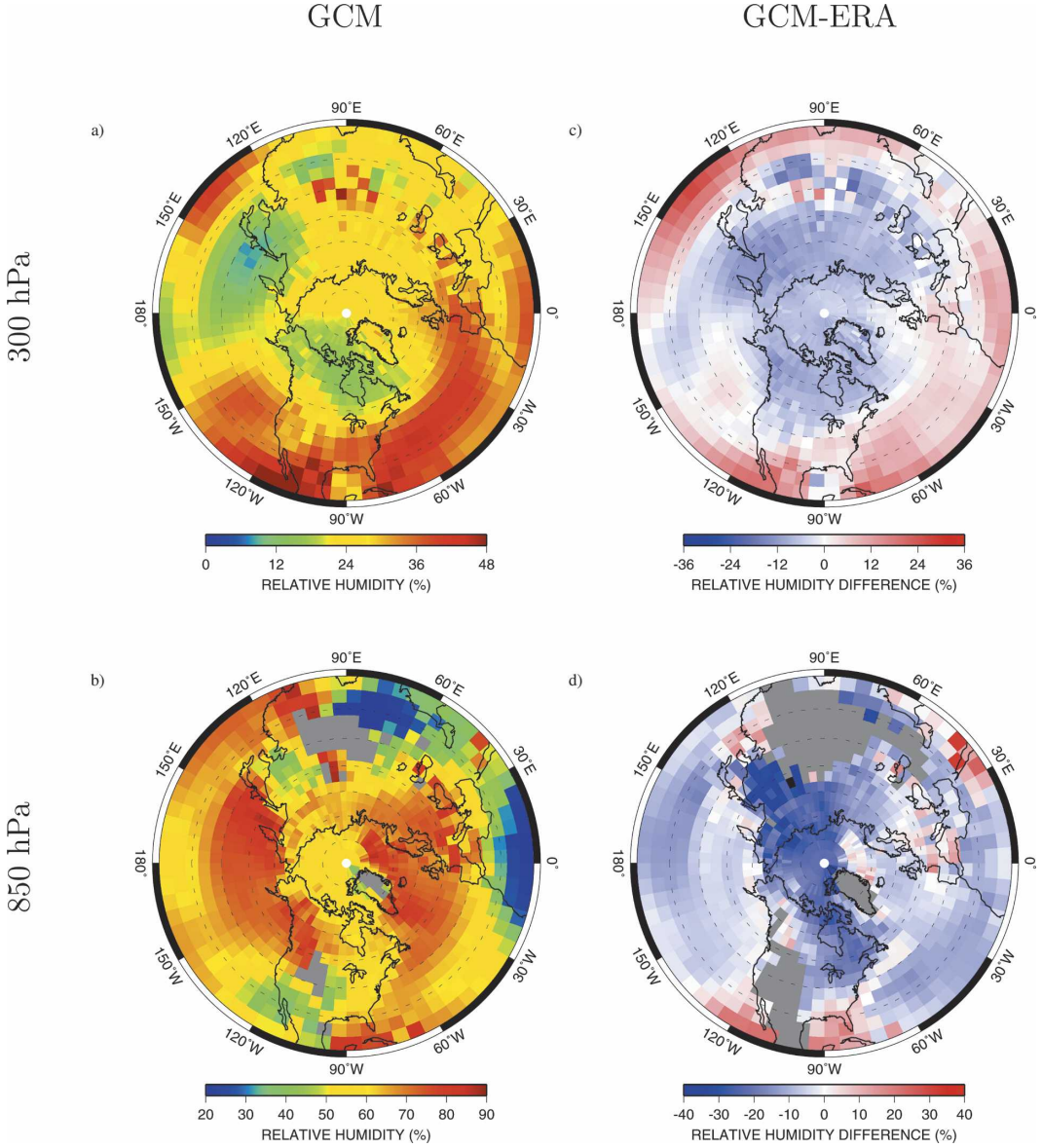

FIG. 3. GISS GCM (a) 300- and (b) 850-hPa climatological DJF relative humidity fields and (c), (d) corresponding GCM–ERA-40 differences. Gray shading denotes topographic intersections with constant pressure surfaces. The reanalysis was interpolated to the GCM grid prior to differencing.

that the GCM is drier than ERA-40 over the eastern oceans, especially the Atlantic, which actually puts it into better agreement with NVAP. Over the Pacific storm track, both the GCM and ERA-40 have a low-level moist bias at the southern edge and are too dry at the northern edge.

4. Cyclone statistics

The generally realistic GCM mean humidity field hides compensating errors that occur on shorter time scales within cyclone regions. One clue to GCM shortcomings can be obtained by examining how often GCM cyclones occur. Figure 4 shows the frequency distribution of cyclones for the GCM, ERA-40, and NRA. GCM cyclones are less frequent (~600 versus ~900 per decade) and less intense (by ~20%) than are those found in the two reanalyses, whose distributions closely resemble each other. The GCM–reanalysis differences occur to some extent in the intermediate intensity category, but most obviously for strong storms (<5% of GCM storms exceed the intensity threshold that classi-

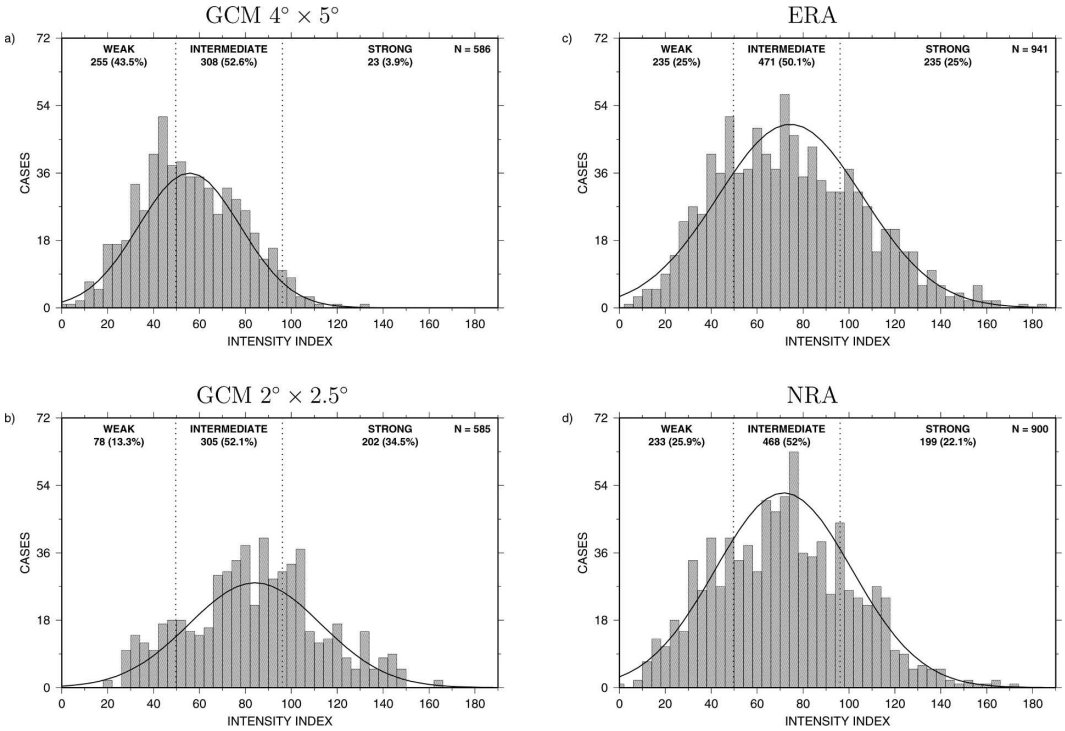

FIG. 4. Frequency histograms of DJF cyclone occurrence as a function of intensity index in the GISS GCM at (a) 4° × 5° × 23 layer resolution and at (b) 2° × 2.5° × 32 layer resolution, and in the (c) ERA-40 and (d) NRA reanalyses. The statistics for the 2° × 2.5° × 32 layer GCM come from only 4 winters and have been projected to 10 winters to facilitate comparison with the other histograms.

fies 25% of ERA-40 cyclones as strong). We also find that the GCM produces far fewer rapid deepening or "bomb" cyclones as well, these being defined as cyclones with a sustained 1 hPa h^{-1} decrease in central pressure over 24 h after being geostrophically adjusted to 60°N (Sanders and Gyakum 1980).

One possible interpretation of these results is that the GCM's coarse resolution limits cyclogenesis. Four winters of a higher-resolution (2° × 2.5° × 32 layers) run of a slightly earlier version of the GCM (Hansen et al. 2002) were available, though only at 12-h resolution and with only SLP information. We applied the cyclone-tracking algorithm to this run as well. The results, also shown in Fig. 4, indicate that the higher-resolution model produces storms that are on average ~50% stronger, but this occurs at the expense of weak storms (i.e., higher resolution does not increase the total number of storms). Resampling the 4° × 5° GCM at 12-h intervals suggests that some of the shortfall in weak storms in the 2° × 2.5° model may be due to the sampling, with perhaps a 5%–10% underestimate in overall storm frequency remaining relative to the reanalyses.

Figure 5 shows the spatial distribution of cyclone frequency of occurrence in the GCM and the difference with respect to ERA-40. The GCM produces storm tracks in approximately the same locations as ERA-40 but underpredicts the frequency along the east coasts of both continents and especially in the subpolar lows. Moreover, those GCM cyclones that do reach the subpolar lows also spend less time there (Bauer 2005). The GCM also produces virtually no storms in the southeastern United States, an important region for North American cyclogenesis. The reanalysis time period we analyze was one of generally (and sometimes strongly) positive Arctic/North Atlantic Oscillation (AO/NAO) index, while the GCM with climatological SSTs simulates a pattern like that for a strong negative AO/NAO index. A negative index, with a weak Azores high and weak Icelandic low, is characterized by fewer and weaker North Atlantic cyclones and a more equatorward and zonally oriented North Atlantic storm track (cf. Hurrell et al. 2003). However, comparisons with reanalysis results from a strong negative AO/NAO period (1959–69) suggest that this phase offset accounts for at most 5% of the total GCM-reanalysis cyclone difference seen in Fig. 5.

A more likely reason for the cyclone deficiency in the GCM is secondary cyclogenesis, for example, due to frontal waves. We repeated our analysis but doubled the search radius used to isolate individual cyclones;

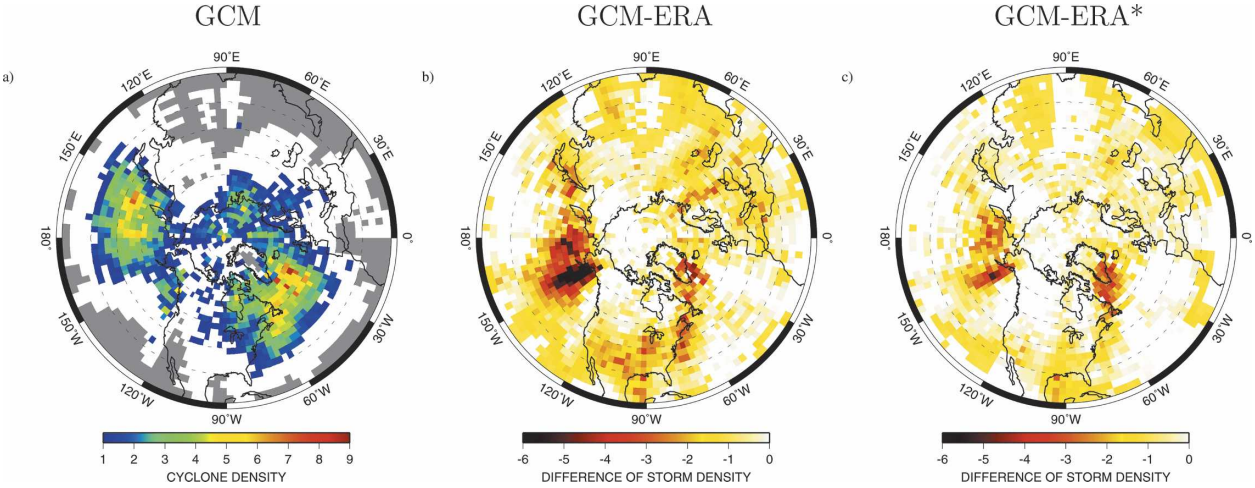

FIG. 5. Climatological DJF cyclone density (number per month) projected onto a 4° × 5° grid from statistics collected on an equal area grid. (a) GISS GCM, (b) GCM–ERA-40 difference, and (c) same as in (b) but with storms resulting from secondary cyclogenesis excluded.

this prevents two or more cyclone centers from existing within 1500 km of each other. The reanalysis is much more sensitive to this change, losing about one-third of its cyclones, whereas the GCM loses almost none. In other words, the GCM lacks secondary cyclones. Figure 5c shows that when secondary cyclones are screened out in this way, GCM–ERA-40 differences almost disappear along the coastal storm tracks and are greatly reduced in the Aleutian and Icelandic lows.

As a check on the performance of our cyclone identification and tracking algorithm, we also calculated storm-track activity using an independent technique. Figure 6 shows the GCM and reanalysis 24-h difference-filtered meridional velocity variance at 300 and 850 hPa, a common storm-track diagnostic (Wallace et al. 1988; Chang 2004). Peaks in the GCM 850-hPa variance coincide with those in Fig. 5a, and differences with respect to the reanalysis are similar though somewhat broader in spatial extent, perhaps due to wave packet development and dispersion. GCM–reanalysis differences are even greater at 300 hPa, suggesting that GCM cyclones are too shallow. We explore the reasons for this in section 5.

Another problem with GCM cyclones appears to be related to the placement of the climatological jets and the baroclinicity and strong vertical wind shear associated with them, which makes them regions of peak cyclogenesis (Wang and Fu 2000a). These zones are shifted poleward in the GCM relative to their location in ERA-40 (Fig. 7), and the North American jet is more zonal as well. This implies that GCM cyclogenesis occurs farther from the destabilizing influence of warm, moist subtropical boundary layer air and thus initiates in a colder, drier environment. In fact, the GCM creates fewer than half as many cyclones as ERA-40 between 20° and 40°N. The East Asian jet in particular is also weaker and shorter than observed, implying weaker baroclinicity and cyclogenesis. Several GCM deficiencies contribute to this behavior. Precipitation over the Maritime Continent is weaker than observed and shifted too far north in boreal winter. Thus, the poleward branch of the Hadley cell penetrates to higher latitudes than is realistic at these longitudes. The GCM also has an unrealistic local precipitation maximum over China in winter associated with errors in flow over high topography. Dipole-like surface temperature errors exist over East Asia (Schmidt et al. 2006) but at latitudes that bias the surface baroclinicity in the opposite sense of that needed to explain the weak jet.

5. Cyclone composite structure

Figure 8 shows the composite SLP and lower-, middle-, and upper-troposphere geopotential height fields for intermediate category cyclones at their time of peak intensity in the GCM and ERA-40. The SLP pattern in the GCM generally resembles that of ERA-40 but is more symmetric about the surface low, understating the extensions to the east and southwest that mark the climatological location of warm and cold fronts. In the free troposphere, the GCM produces shallower depressions above the surface low and a less intense wraparound structure to the north and west.

GCM storms also travel ~20% slower than their ERA-40 counterparts and therefore develop and dissipate over a much shorter distance (Fig. 9). This slug-

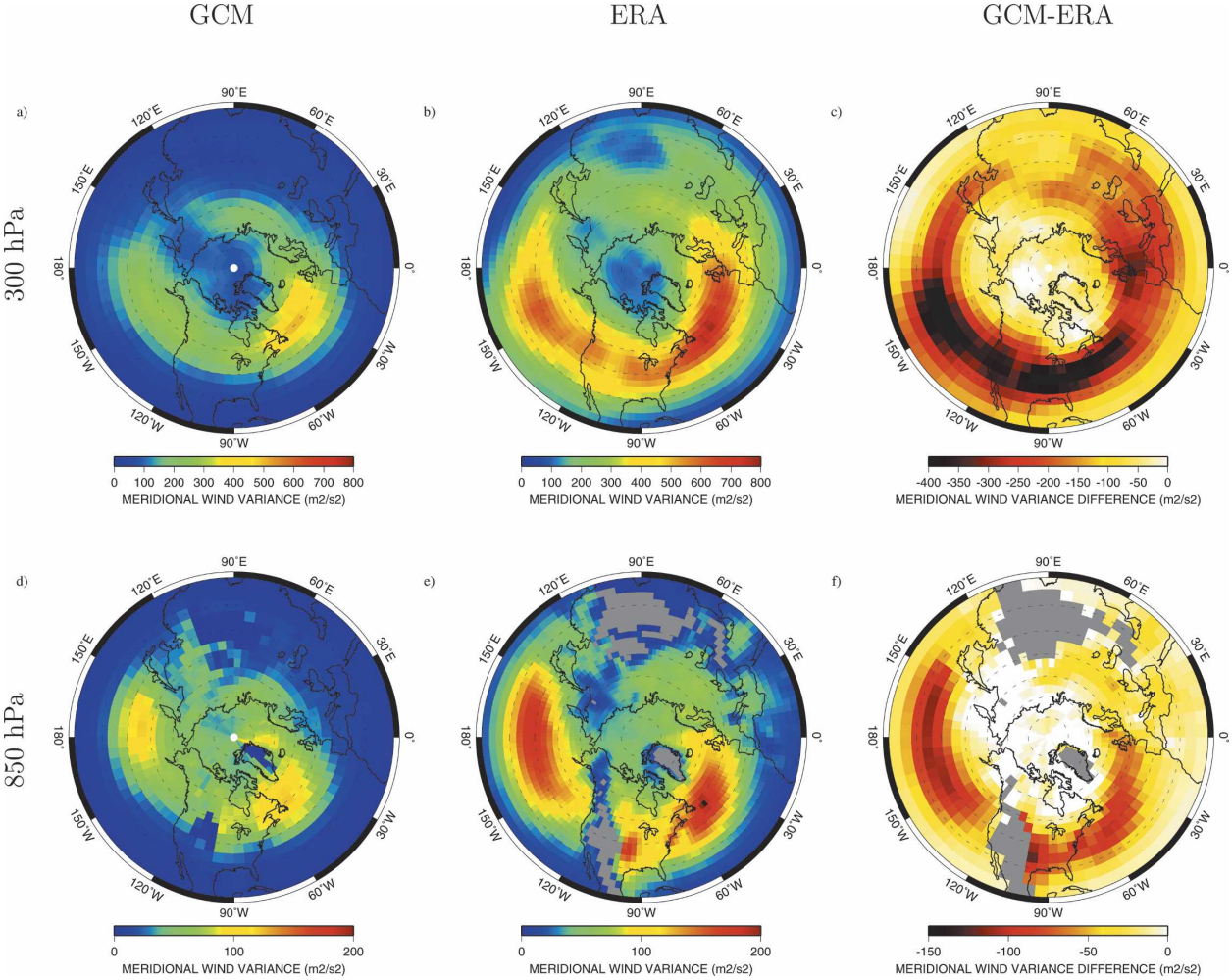

FIG. 6. Climatological 24-h difference-filtered meridional velocity variance ($m^2\ s^{-2}$) at (top) 300 and (bottom) 850 hPa for the (a), (d) GCM, (b), (e) ERA-40, and (c), (f) GCM–ERA-40 difference.

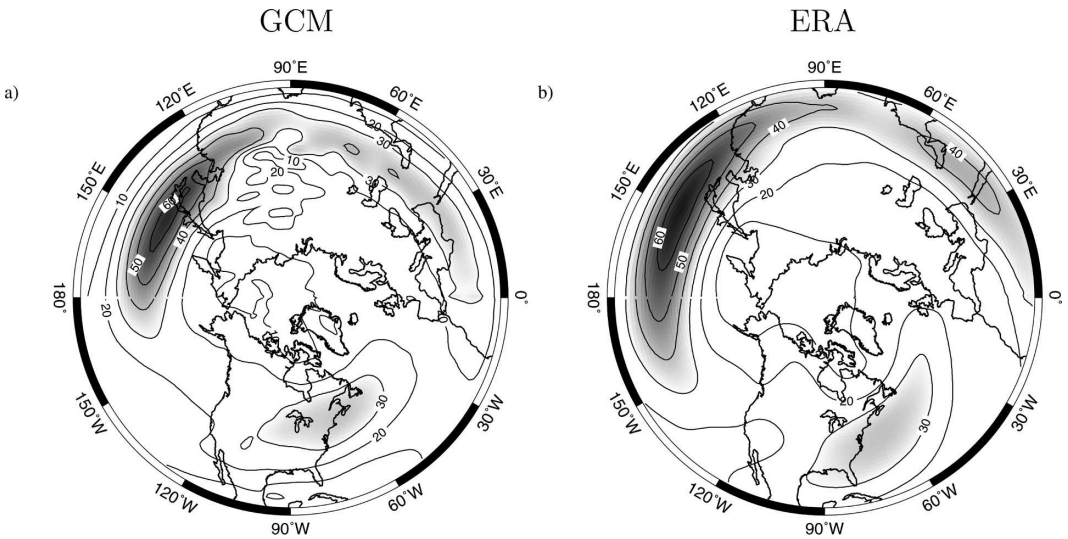

FIG. 7. Climatological DJF 300-hPa horizontal wind speed ($m\ s^{-1}$) in (a) the GCM and (b) ERA-40. Speeds $>30\ m\ s^{-1}$ are shaded.

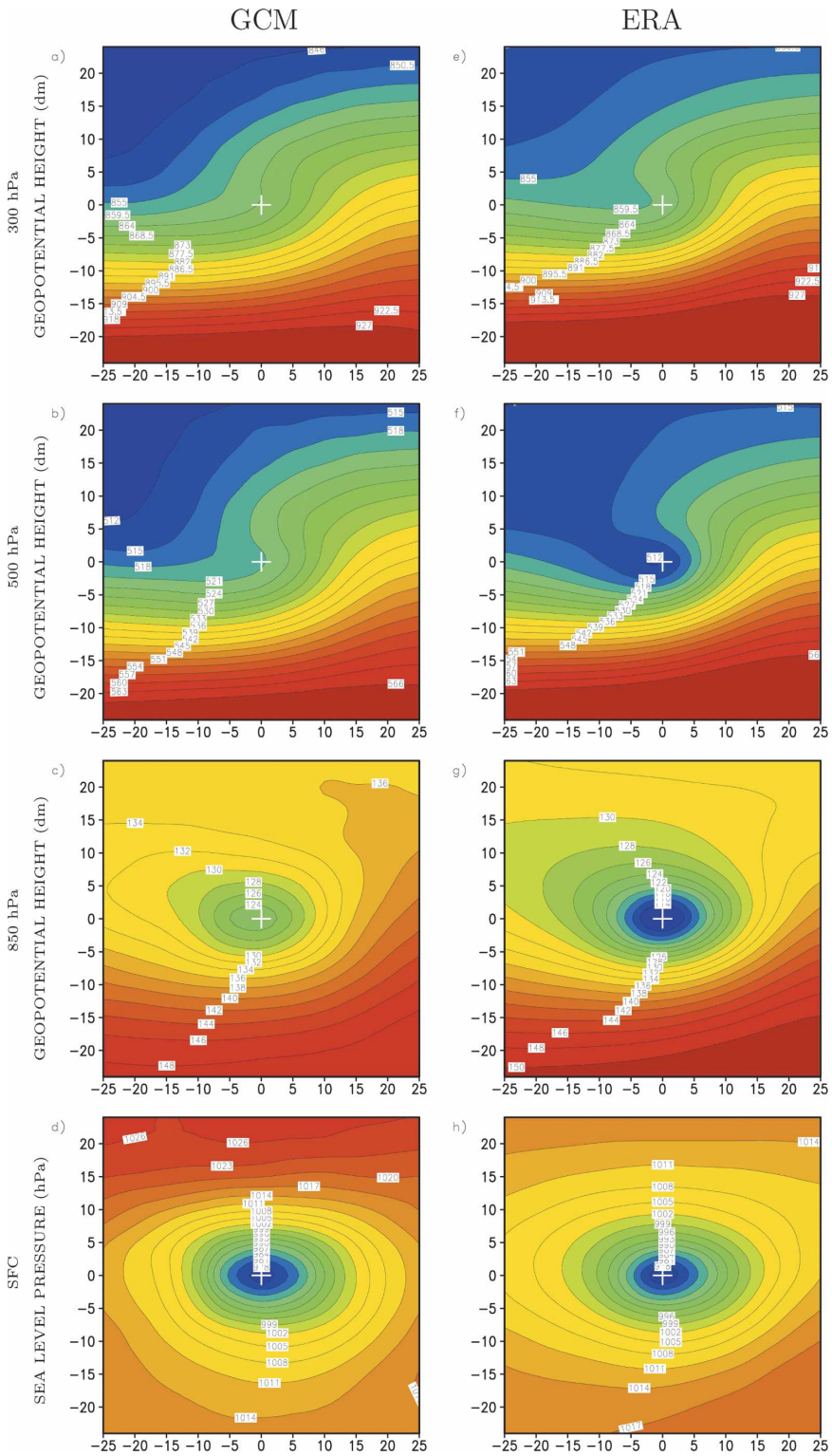

FIG. 8. Composite fields for DJF intermediate strength cyclones at peak intensity. Geopotential height (dam) at (a), (e) 300, (b), (f) 500, (c), (g) 850 hPa, and (d), (h) SLP (hPa), in the (left) GCM and (right) ERA-40. The fields are plotted in a latitude–longitude coordinate system centered on the position of the central SLP minimum of each cyclone (indicated by the +).

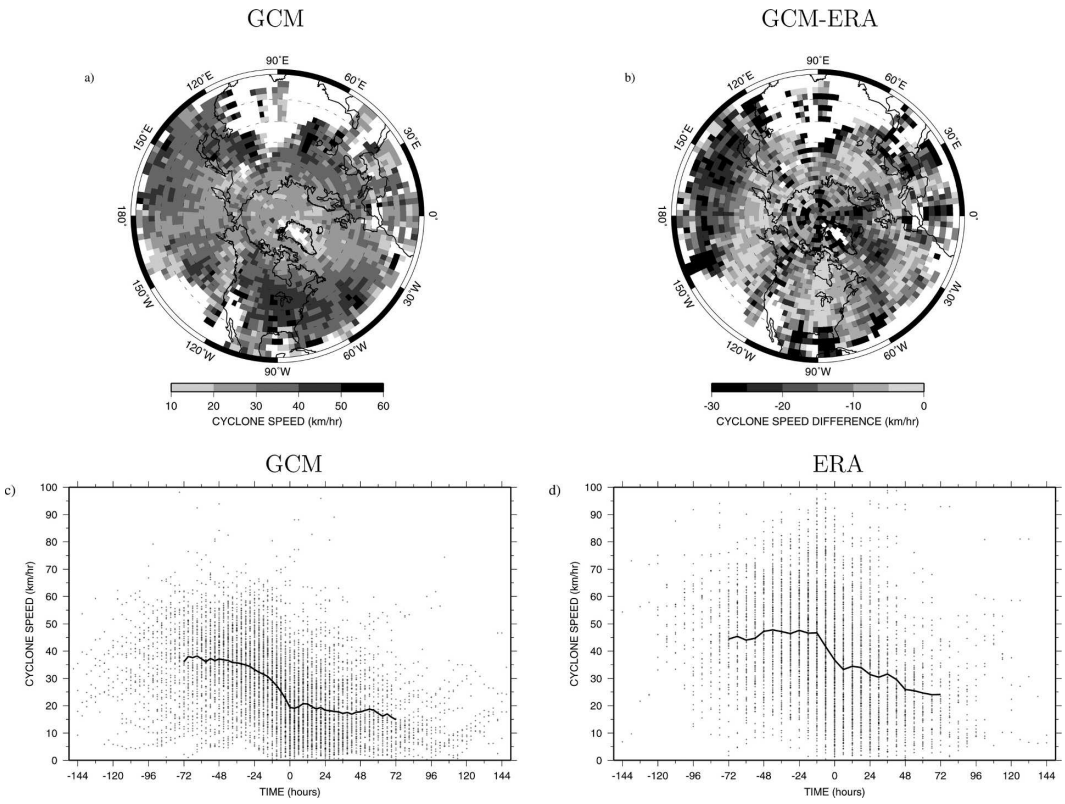

FIG. 9. Climatological DJF average cyclone propagation speed (km h^{-1}) distribution for (a) the GCM and (b) the GCM–ERA-40 difference. Propagation speeds for individual storms vs time (h) relative to the time of minimum SLP for each storm in (c) the GCM and (d) ERA-40. The solid curves represent slightly smoothed averages.

gishness exists almost everywhere but is particularly evident along the south and southeast edges of the primary storm tracks. Cyclones propagate faster in the 2° × 2.5° × 32 layer version of the GCM but are still ~10%–15% slower than ERA-40. Figure 9 also suggests that the GCM–ERA-40 speed difference is greatest during the period of rapid development just before the cyclone reaches peak intensity, when maximum propagation speeds occur in ERA-40 storms but not in GCM storms. GCM cyclones on average begin slowing ~48 h before peak intensity as opposed to ~12 h for ERA-40.

Given the weak geopotential anomalies in the GCM, it is no surprise that the GCM's composite cyclone horizontal wind field is weaker than that in ERA-40 (Figs. 10a–f). Cyclone winds in the GCM are also more zonal than those in ERA-40, consistent with its weaker meridional velocity variance (Fig. 6), implying that meridional water vapor transports by the warm conveyor belt are less effective than in actual storms. This is tied to an apparently weak ageostrophic circulation in GCM cyclones. Figures 10g–l show that the GCM vertical velocity (ω) field is almost 3 times weaker than that of ERA-40 in ascending regions in the lower troposphere, lacks the midtroposphere maximum that ERA-40 storms have, and is barely evident at 300 hPa, that is, GCM storms are shallower than ERA-40 storms. ERA-40 ascending regions also extend east of the surface low at low levels and tilt farther eastward from the low in the upper troposphere, while the GCM's ageostrophic circulation is almost upright, with peak ascending motion over the surface low at all levels. The long tongue of upward motion that extends south and west of the low in ERA-40, marking the cold front, is present only in abbreviated form in the GCM. GCM descending motions are spread over a broad region mostly west of the low rather than being concentrated southwest of the low, behind the surface cold front, as is seen in the ERA-40 composite.

The slow movement of GCM storms is consistent with its weaker geopotential height anomalies and vertical motion, according to quasigeostrophic dynamics (cf. Holton 1992, p. 177). Slow-moving storms have weaker ω forcing and thus weaker vertical motions near the cyclone. Indeed, we find a positive correlation between peak ascending motion and cyclone propagation

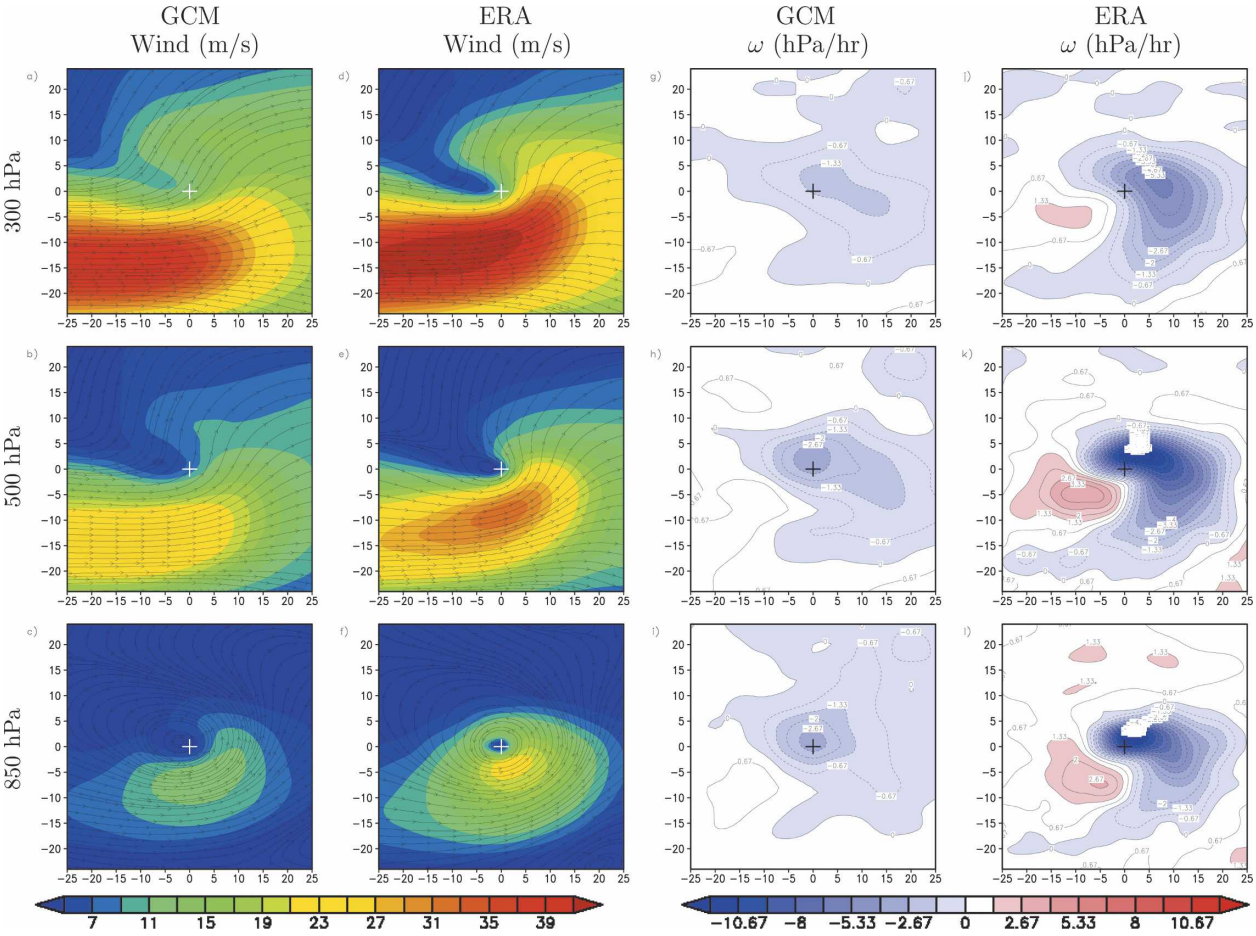

FIG. 10. Intermediate cyclone composite horizontal wind (m s^{-1}) fields for the (a), (b), (c) GCM and (d), (e), (f) ERA-40 and vertical velocity ω (hPa h^{-1}) fields for the (g), (h), (i) GCM and (j), (k), (l) ERA-40 at (top) 300, (middle) 500, and (bottom) 850 hPa. The colors show speeds and the curves indicate streamlines in (a)–(f).

speed in the ERA-40 and NRA storm populations, but not in that of the GCM (Bauer 2005). Favorable conditions for rising motions are produced by warm low-level advection coupled with differential advection of positive (cyclonic) vorticity. Both of these are weaker in the GCM than in the reanalysis, resulting in weaker SLP tendencies east and north of the surface low 12 h before peak storm intensity (Fig. 11).

The composite temperature field of the GCM (Figs. 12a–f) reflects all the dynamical deficiencies described above, and in addition shows an overall 2–3-K cold bias relative to the ERA-40 composite at all levels and a weaker meridional temperature gradient at upper levels, consistent with the weak jets in cyclogenesis regions (Fig. 7). The combined result of all these effects is an anemic composite pattern of cyclone humidity advection (Figs. 12g–l). Positive (negative) humidity tendencies primarily due to upward (downward) motion east and north (south and west) of the low are 2–3 times stronger in ERA-40 than in the GCM in the lower and middle troposphere. In the upper troposphere, GCM cyclones are barely a source of humidity at all, whereas ERA-40 cyclones moisten upper levels over a broad region because of both horizontal and vertical transports along the warm conveyor belt. The resulting cyclone composite relative humidity fields in the GCM (Figs. 13a–f) indicate an overall ~5% low bias relative to ERA-40, with less frontal organization, that is, humidity extremes in GCM storms are not as moist or dry as those in ERA-40. Combined with the effect of the GCM cold bias, the GCM composite specific humidity field (Figs. 13g–l) shows water vapor deficiencies of as much as a factor of 2 in the middle and upper troposphere east of the surface low. Thus, not only do GCM cyclones occur too infrequently, but in addition they do not move enough moisture poleward and upward when they do occur.

The coarse resolution of climate GCMs is a likely

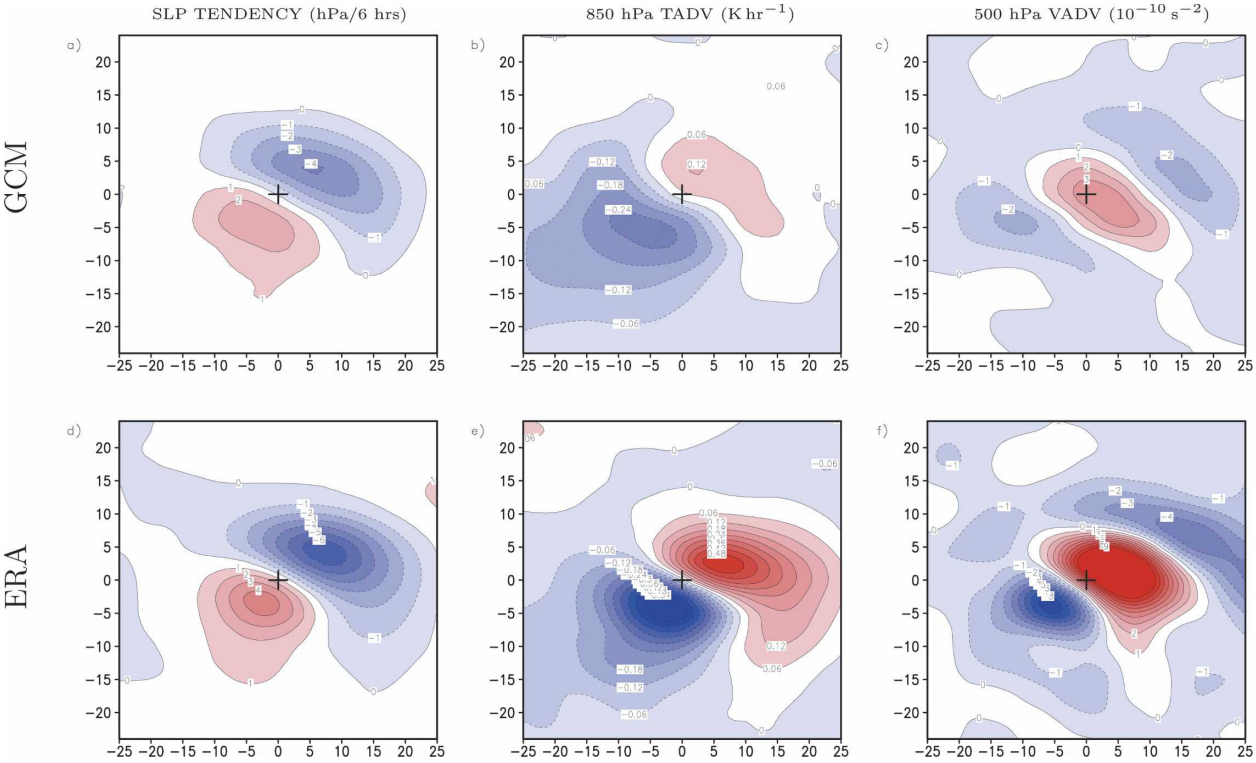

FIG. 11. Intermediate cyclone composite (a), (d) SLP tendency (change over the following 6 h, hPa), (b), (e) 850-hPa temperature advection (K h^{-1}), and (c), (f) 500-hPa vorticity advection (10^{-10} s^{-2}) for the (top) GCM and (bottom) ERA-40 at a time 12 h before reaching peak intensity.

source of these errors, since these models do not resolve the sharp temperature gradients on frontal scales that are so important to cyclone development. The weakness of the GCM's climatological jets on larger scales (Fig. 7) must be another important factor. However, latent heat release in frontal zones is a nonnegligible, if secondary, contributor to the generation of eddy available potential energy (Manobianco 1989), and precipitation is a major moisture sink. Thus, it is possible that the GCM's problems are associated with cloud and precipitation parameterization deficiencies. We tested this hypothesis in two ways. First, we compared the GCM cyclone composite precipitation field for storms of different strengths to those produced by both reanalyses and derived from an experimental 3-hourly global precipitation dataset (Huffman et al. 2003). The results are shown in Fig. 14. ERA-40 and NRA have fairly similar composite precipitation structure, with ERA-40 producing somewhat stronger precipitation for weak and intermediate storms and a more northward displacement of the precipitation maximum relative to NRA. The precipitation dataset composite (which consists of only three winters and is therefore noisier) shows similar maximum composite precipitation rates but heavier rain east of the surface low than either reanalysis. GCM composite precipitation rates, by comparison, are weaker, the discrepancy becoming greater as storm strength increases. GCM precipitation is also less organized around strong storms. Thus, the GCM is certainly not too dry because its convection and microphysics parameterizations overestimate rainfall.

On the other hand, if the GCM parameterizations underestimate rainfall early in the storm life cycle, this might suppress further development of the storm (cf. Miller and Petty 1998). If this were the case, we might expect to see more realistic GCM storm structure in the early stages of growth, when diabatic heating has not yet become important and the only source of available potential energy is the resolved baroclinicity. Figure 15 compares a variety of GCM and ERA-40 300-hPa composite fields for intermediate cyclones acquired at the moment the storm was first detected by the tracking algorithm (i.e., when it first formed closed isobars).

First, we note that the GCM lacks a prominent short wave to the northwest of the surface low compared to ERA-40 (Figs. 15a,d). The greater upper-level support present in ERA-40 storms must contribute to their deeper structure, as evidenced by their stronger upper-level vertical velocities at initiation (Figs. 15b,e). An-

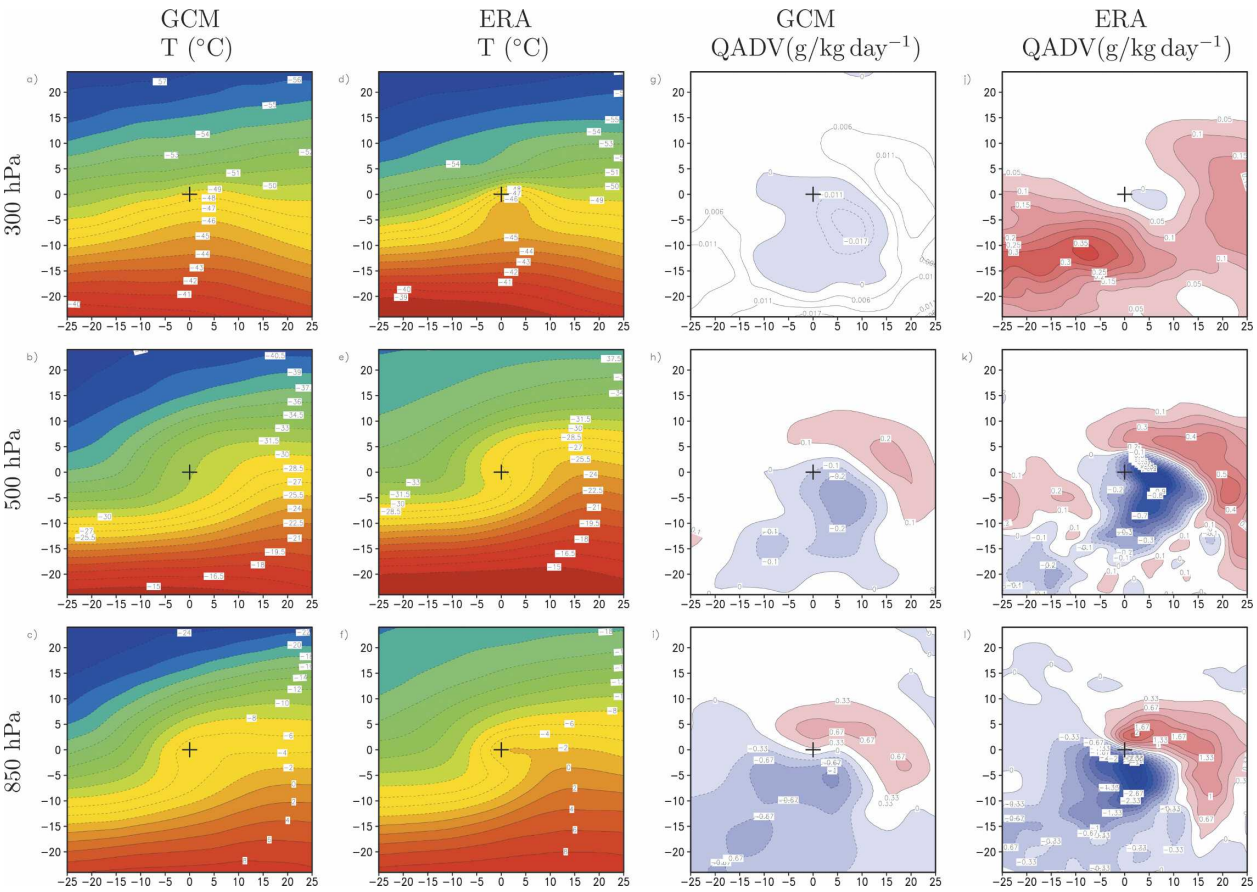

FIG. 12. Same as in Fig. 10 but for temperature (°C) and specific humidity advection (g kg^{-1} day^{-1}).

other early stage difference is that jet streaks (localized wind speed maxima along the jet stream) are much more obvious in ERA-40 cyclones than in GCM cyclones (Figs. 15c,f). The placement of ERA-40 jet maxima relative to the surface low is such as to have the most influence on cyclogenesis and storm development; furthermore, the streamlines exiting the jet maxima curve cyclonically and are diffluent, which strongly favors ascending motions near the left-exit region (cf. Keyser and Shapiro 1986). This is consistent with the location of the ERA-40 composite upward motion maximum north and east of the exit region (Fig. 15e). The GCM jet maximum, by comparison, is weaker, straighter, and less diffluent, which must also contribute to its weaker upper-level vertical motion field (Fig. 15b).

Thus, we conclude that the dynamic conditions required for cyclone development are more favorable from the outset in ERA-40 than in the GCM, regardless of any parameterization deficiencies that may exist. Associated with this, ERA-40 humidity fields (Figs. 15j,k) are more organized with more humid air penetrating poleward, and ERA-40 temperature fields exhibit greater baroclinicity (Fig. 15l) than their GCM counterparts (Figs. 15g,h,i) even at storm initiation.

6. Discussion

We have used reanalysis products in place of direct observations because composite analysis requires a comprehensive space–time sample of atmospheric conditions not available from observations. In so doing we are assuming that reanalysis fields adequately represent the characteristics of real-world extratropical cyclones. For some quantities, such as SLP, this is the case (cf. Kalnay et al. 1996), especially over well-observed continental areas of the midlatitudes. Over the more data-sparse midlatitude oceans, however, some nonnegligible errors can be expected due to both initialization errors for forecasts and inadequacies of the forecasting models themselves. For example, McMurdie and Mass (2004) found that an NCEP weather model produced systematic forecasting errors in the position and central pressure of wintertime cyclones as they came ashore

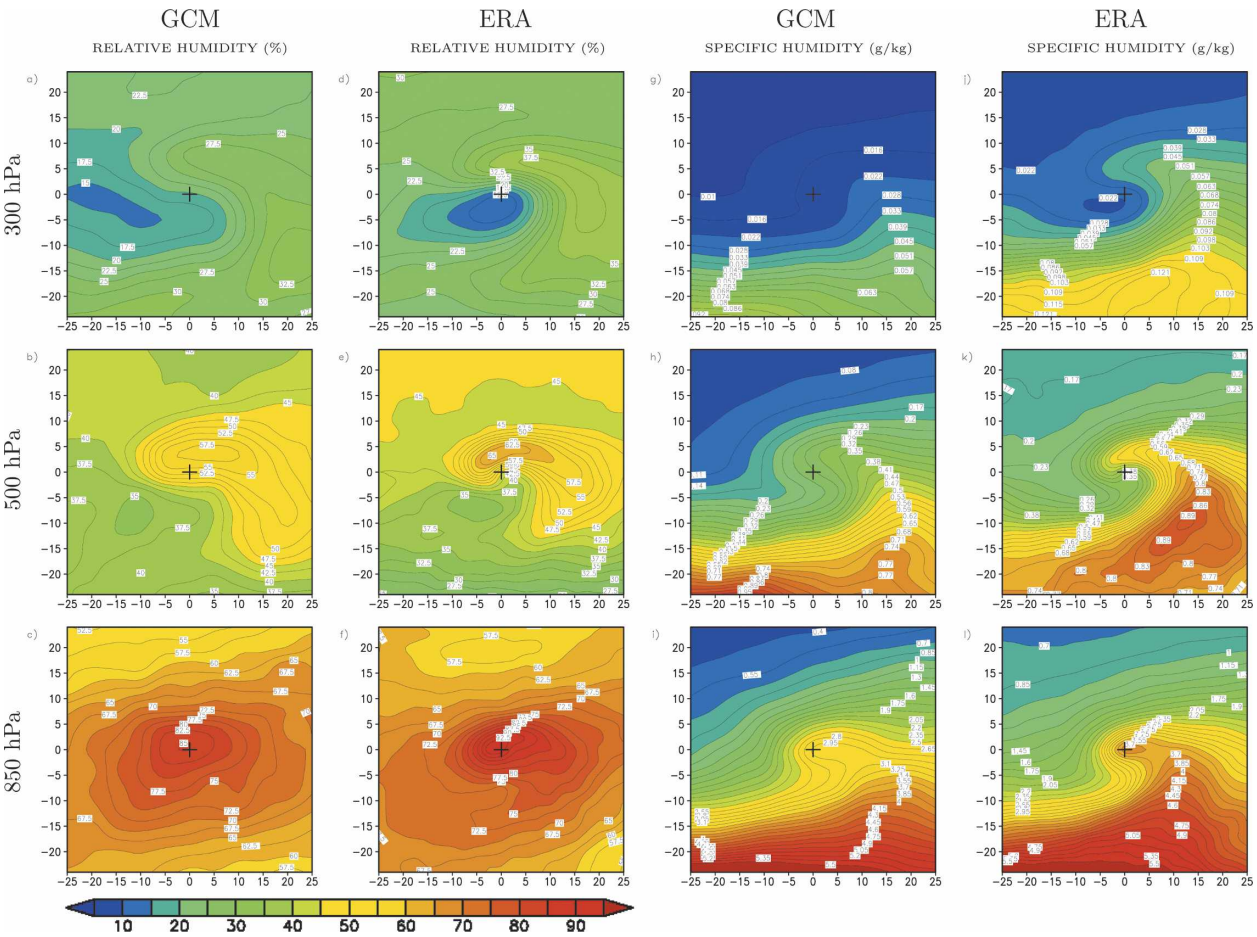

FIG. 13. Same as in Fig. 10 but for relative humidity (%) and specific humidity (g kg^{-1}).

near Washington State from the relatively data-poor North Pacific. Even over the data-rich United States, the mesoscale Rapid Update Cycle-2 model analysis underestimates vertical velocities in precipitating weather systems (Xie et al. 2004). Nonetheless, the composite cyclone structure we derive for reanalysis dynamical fields is consistent with the classical well-observed features of extratropical storms, and we therefore judge it to be a useful standard of comparison.

Using the reanalysis composite dynamical fields as a guide, then, we conclude that cyclone vertical motion, and hence the ageostrophic circulation, in the GISS GCM and most likely other climate GCMs, is underestimated. This has consequences not only for storm development, propagation speeds, and precipitation, but also for the water vapor and cloud fields associated with GCM cyclones. Our analysis shows that GCM cyclones lack the classical tilted frontal structure that is present in the ERA-40 composites. Frontal tilt is the distinguishing feature of semigeostrophic frontogenesis, the tilt being produced by advection of thermal fields by the ageostrophic circulation (cf. Houze 1993, 451–459). In the GCM, the ageostrophic flow is so weak that storm development more closely resembles quasigeostrophic frontogenesis, in which only advection by the geostrophic flow is included and the resulting advection can sharpen frontal boundaries but cannot change their orientation. Frontal tilt in semigeostrophic dynamics increases with baroclinicity (Hakim and Keyser 2001), which is too weak in the GCM's cyclogenesis regions as evidenced by its deficient jets (Fig. 7).

As a consequence, the GCM tends to produce an excess of high-top, optically thick clouds over a small area in midlatitude storms and a deficit of clouds that are optically thinner or that have tops at midlevels (Tselioudis and Jakob 2002; Del Genio et al. 2005). The fact that all climate GCMs have the same cloud-type biases despite their very different cloud parameterizations (Zhang et al. 2005) suggests that the so-called resolved dynamics of climate GCMs are not actually adequately resolved for climate applications. Of spe-

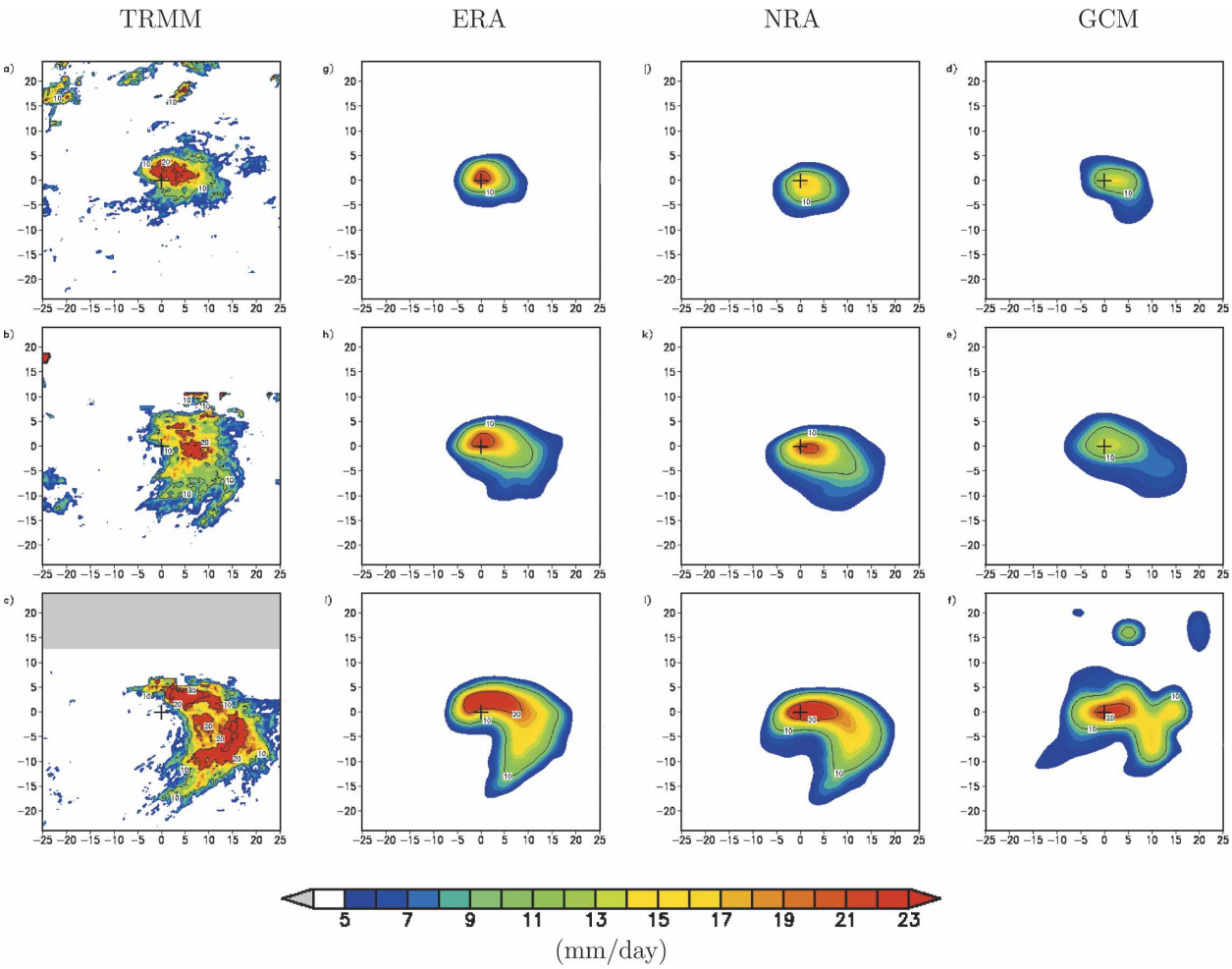

FIG. 14. Composite cyclone precipitation (mm day^{-1}) fields for (top) weak, (middle) intermediate, and (bottom) strong storms for (a), (b), (c) the TRMM multisatellite retrieval, (d), (e), (f) ERA-40, (g), (h), (i) NRA, and (j), (k), (l) the GCM.

cific concern to the GISS GCM is its weak upper-level vertical motion and humidity advection centered primarily above the surface low. ERA-40 instead produces a broad region of upper-level ascent and humidity advection east of the surface low that is conducive to generating the type of extensive ridge-crest and baroclinic leaf cirrus shields that have been observed in field experiments (cf. Starr and Wylie 1990; Mace et al. 1995). The GCM instead lacks the dynamical moisture sources from below and from warmer, more humid areas to the southwest and can thus make cirrus only in a limited area for a given storm. Coupled with the GCM's underestimate of storm occurrence, its midlatitude cirrus deficiency can be attributed to dynamical rather than parameterization inadequacies. The GCM exhibits weak vertical velocities of both signs and thus produces a narrower humidity distribution than ERA-40. In this way the apparent realism of the GCM's mean humidity field (Fig. 3) hides errors in variability (Fig. 13) that determine the cloud fraction.

To some extent these deficiencies might be addressed indirectly via parameterization, for example, by assuming minimum cloud overlap in diagnosed frontal regions. It might even be possible to diagnose the unresolved sharpening of grid-scale fronts in developing cyclones and to parameterize the resulting subgrid ageostrophic motion response, including horizontal transport between grid boxes that generates frontal tilt. Ultimately, though, higher resolution is needed. Our results suggest that increasing the GCM resolution to 2° $\times$ 2.5° $\times$ 32 layers, comparable to that of most current climate GCMs, does produce somewhat more and faster storms, but this model still falls short of observed storm behavior (and has only a minimal positive impact on upper-level humidity). Further resolution increases might allow the GCM to produce stronger temperature

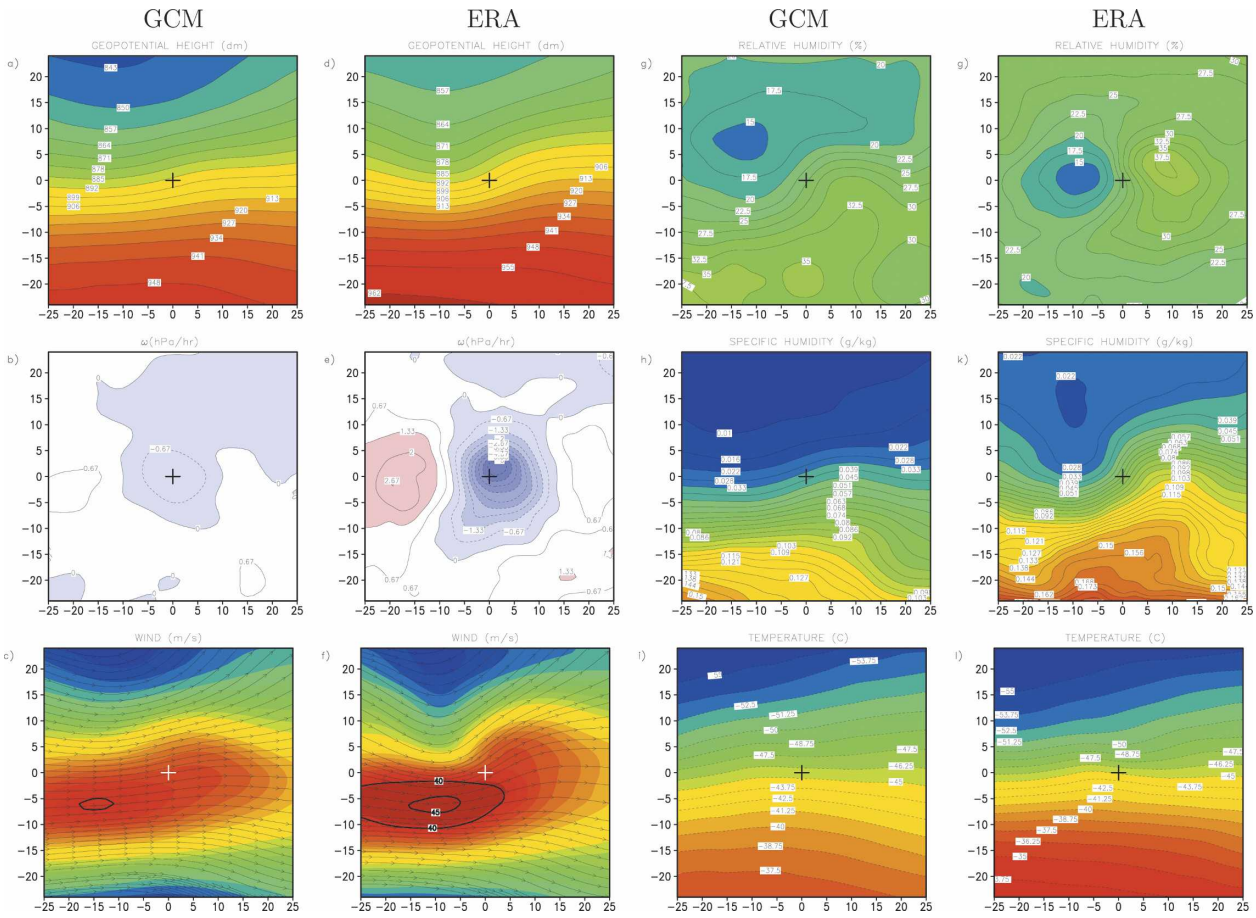

FIG. 15. Intermediate cyclone composite fields at 300 hPa acquired at the time each cyclone was first detected by the storm-tracking algorithm. (a), (b), (c) Geopotential height (dam), ω (hPa h^{-1}), and horizontal wind (m s^{-1}) in the GCM. (d), (e), (f) Same as in (a)–(c) but for ERA-40. (g), (h), (i) Relative humidity (%), specific humidity (g kg^{-1}), and temperature (K) for the GCM. (j), (k), (l) Same as in (g)–(i) but for ERA-40.

gradients and jet speeds. Conaty et al. (2001) show that halving or quartering the resolution of a 2° × 2.5° model tangibly improves the structure and development of a GCM's baroclinic cyclones by resolving sharp frontal and other surfaces more accurately. This favors the type of secondary cyclogenesis missing from the GCM, which is sparked by instabilities along the intense frontal boundaries of strong mature parent cyclones (Ayraul et al. 1995; Parker 1998). Current computational resources should make this a reasonable short-term goal for many climate GCM groups. In addition, finer resolution should enable climate GCMs to better maintain the highly baroclinic upper-level conditions necessary for the development of jet streaks, which induce stronger vertical motion and link surface development more closely with that aloft.

It is also possible that our experimental setup using climatological SSTs contributes to some apparent deficiencies in the GCM water vapor distribution. Unchanging seasonal SSTs will dampen the otherwise large changes in the position and strength of the East Asian jet, a locus of peak cyclogenesis and a guide to the North Pacific storm track (Yang et al. 2002). In addition to being more fixed in location and steady in time, this jet is also farther north in the GCM than in the reanalyses (cf. Fig. 7). Variations in the East Asian jet are known to influence the distribution and variability of mid- to upper-level water vapor across much of the North Pacific (Wang and Fu 2000a,b). The dry bias the GCM exhibits in this region (Fig. 3) may be related to this difference. Our experiment also lacks the ENSO interannual variability that may affect subtropical upper-level humidity through changes in the westerly duct and meridional water vapor transports (Cohen et al. 2000; Bates et al. 2001).

Whether or not the GCM's extratropical cyclone biases degrade its climate forecasts is an open issue. However, given the systematic problems revealed in this

study, and the probability of similar deficiencies in other climate GCMs, we suggest that inferences about climate changes in the frequency and strength of midlatitude cyclones (cf. Carnell and Senior 1998) be viewed with caution. Likewise, impacts associated with such changes (e.g., predictions of regional temperature changes and trends in drought/flood occurrence and severity in midlatitudes) should also not be trusted until baroclinic cyclones, the major cloud producers and synoptic-scale organizers of midlatitude precipitation, can be simulated with greater fidelity.

Acknowledgments. The authors thank Mark Chandler, Jeff Jonas, and Max Kelley for helpful discussions. Greg Hakim and an anonymous reviewer provided useful suggestions that improved the original manuscript. This research was supported by the NASA Radiation Sciences, NASA Precipitation Measurement Missions, and DOE Atmospheric Radiation Measurement Programs.

REFERENCES

Ayraul, F., F. Lalaurette, A. Joly, and C. Loo, 1995: North Atlantic ultra high frequency variability. *Tellus,* **47A,** 671–696.

Bates, J., D. Jackson, F.-M. Bréon, and Z. Bergen, 2001: Variability of tropical upper-tropospheric humidity 1979–1998. *J. Geophys. Res.,* **106,** 32 271–32 281.

Bauer, M., 2005: Observed and simulated humidity variations. Ph.D. dissertation, Columbia University, 231 pp.

Bengtsson, L., K. Hodges, and S. Hagemann, 2004: Sensitivity of large-scale atmospheric analyses to humidity observations and its impact on the global water cycle and tropical and extratropical weather systems in ERA-40. *Tellus,* **56A,** 202–217.

Blender, R., and M. Schubert, 2000: Cyclone tracking in different spatial and temporal resolutions. *Mon. Wea. Rev.,* **128,** 377–384.

——, K. Fraedrich, and F. Lunkeit, 1997: Identification of cyclone-track regimes in the North Atlantic. *Quart. J. Roy. Meteor. Soc.,* **123,** 727–741.

Browning, K. A., 1999: Mesoscale aspects of extratropical cyclones: An observational perspective. *The Life Cycles of Extratropical Cyclones*, M. Shapiro and S. Grønås, Eds., Amer. Meteor. Soc., 265–283.

Carlson, T., 1998: *Mid-Latitude Weather Systems*. Amer. Meteor. Soc., 507 pp.

Carnell, R. E., and C. A. Senior, 1998: Changes in mid-latitude variability due to increasing greenhouse gases and sulphate aerosols. *Climate Dyn.,* **14,** 369–383.

Chandler, M., and J. Jonas, cited 1999: Atlas of extratropical storm tracks (1961–1998). NASA Goddard Institute for Space Studies Tech. Rep. [Available online at http://www.giss.nasa.gov/data/stormtracks.]

Chang, E. K. M., 2004: Are the Northern Hemisphere winter storm tracks significantly correlated? *J. Climate,* **17,** 4230–4244.

——, and Y. Fu, 2002: Interdecadal variations in Northern Hemisphere winter storm-track intensity. *J. Climate,* **15,** 642–658.

Cohen, J., D. Salstein, and R. Rosen, 2000: Interannual variability in the meridional transport of water vapor. *J. Hydrometeor.,* **1,** 547–553.

Conaty, A. L., J. C. Jusem, L. Takacs, D. Keyser, and R. Atlas, 2001: The structure and evolution of extratropical cyclones, fronts, jet streams, and the tropopause in the GEOS general circulation model. *Bull. Amer. Meteor. Soc.,* **82,** 1853–1867.

Cooper, O. R., and Coauthors, 2001: Trace gas signatures of the airstreams within North Atlantic cyclones: Case studies from the NARE '97 aircraft intensive. *J. Geophys. Res.,* **106,** 5437–5456.

Cotton, W. R., G. A. Alexander, R. Hertenstein, R. Walko, R. McAnelly, and M. Nicholls, 1995: Cloud venting: A review and some new global annual estimates. *Earth-Sci. Rev.,* **39,** 169–206.

Del Genio, A. D., M.-S. Yao, W. Kovari, and K. K.-W. Lo, 1996: A prognostic cloud water parameterization for global climate models. *J. Climate,* **9,** 270–304.

——, A. B. Wolf, and M.-S. Yao, 2005: Evaluation of regional cloud feedbacks using single-column models. *J. Geophys. Res.,* **110,** D15S13, doi:10.1029/2004JD005011.

Eckhardt, S., A. Stohl, H. Wernli, P. James, C. Forster, and N. Spichtinger, 2004: A 15-year climatology of warm conveyor belts. *J. Climate,* **17,** 218–237.

Gulev, S., O. Zolina, and S. Grigoriev, 2001: Extratropical cyclone variability in the Northern Hemisphere winter from the NCEP/NCAR reanalysis data. *Climate Dyn.,* **17,** 795–809.

Gyakum, J. R., J. R. Anderson, R. H. Grumm, and E. L. Gruner, 1989: North Pacific cold-season surface cyclone activity: 1975–1983. *Mon. Wea. Rev.,* **117,** 1141–1155.

Hakim, G. J., 2003: Developing wave packets in the North Pacific storm track. *Mon. Wea. Rev.,* **131,** 2824–2837.

——, and D. Keyser, 2001: Canonical frontal circulation patterns in terms of Green's functions for the Sawyer-Eliassen equation. *Quart. J. Roy. Meteor. Soc.,* **127,** 1795–1814.

Hansen, J., and Coauthors, 2002: Climate forcings in Goddard Institute for Space Studies SI2000 simulations. *J. Geophys. Res.,* **107,** 4347, doi:10.1029/2001JD001143.

——, and Coauthors, 2005: Efficacy of climate forcings. *J. Geophys. Res.,* **110,** D18104, doi:10.1029/2005JD005776.

Holton, J. R., 1992: *An Introduction to Dynamical Meteorology.* 3d ed. Academic Press, 507 pp.

Houze, R. A., Jr., 1993: *Cloud Dynamics.* Academic Press, 573 pp.

Huffman, G. J., R. F. Adler, E. F. Stocker, D. T. Bolvin, and E. J. Nelkin, 2003: Analysis of TRMM 3-hourly multi-satellite precipitation estimates computed in both real and post-real time. Preprints, *12th Conf. on Satellite Meteorology and Oceanography,* Long Beach, CA, Amer. Meteor. Soc., CD-ROM, P4.11.

Hurrell, J., Y. Kushnir, M. Visbeck, and G. Ottersen, 2003: Overview of the North Atlantic oscillation. *The North Atlantic Oscillation: Climate Significance and Environmental Impact, Geophys. Monogr.,* No. 134, Amer. Geophys. Union, 1–35.

Kalnay, E., and Coauthors, 1996: The NCEP/NCAR 40-Year Reanalysis Project. *Bull. Amer. Meteor. Soc.,* **77,** 437–471.

Keyser, D., and M. Shapiro, 1986: A review of the structure and dynamics of upper-level frontal zones. *Mon. Wea. Rev.,* **114,** 452–499.

Kistler, R., and Coauthors, 2001: The NCEP–NCAR 50-Year Reanalysis: Monthly means CD-ROM and documentation. *Bull. Amer. Meteor. Soc.,* **82,** 247–267.

Klein, S., and C. Jakob, 1999: Validation and sensitivities of fron-

tal clouds simulated by the ECMWF model. *Mon. Wea. Rev.,* **127,** 2514–2531.

König, W., R. Sausen, and F. Sielmann, 1993: Objective identification of cyclones in GCM simulations. *J. Climate,* **6,** 2217–2231.

Lambert, S., 1996: Intense extratropical Northern Hemisphere winter cyclone events: 1899–1991. *J. Geophys. Res.,* **101,** 21 319–21 325.

——, J. Sheng, and J. Boyle, 2002: Winter cyclone frequencies in thirteen models participating in the Atmospheric Model Intercomparison Project (AMIP1). *Climate Dyn.,* **19,** 1–16.

Lanzante, J., and G. Gahrs, 2000: The "clear-sky bias" of TOVS upper-tropospheric humidity. *J. Climate,* **13,** 4034–4041.

Lau, N.-C., and M. W. Crane, 1995: A satellite view of the synoptic-scale organization of cloud properties in midlatitude and tropical circulation systems. *Mon. Wea. Rev.,* **123,** 1984–2006.

Mace, G. G., D. O'C. Starr, T. P. Ackerman, and P. Minnis, 1995: Examination of coupling between an upper-tropospheric cloud system and synoptic-scale dynamics diagnosed from wind profiler and radiosonde data. *J. Atmos. Sci.,* **52,** 4094–4127.

Manobianco, J., 1989: Explosive east coast cyclogenesis over the west-central North Atlantic Ocean: A composite study derived from ECMWF operational analyses. *Mon. Wea. Rev.,* **117,** 2365–2383.

McMurdie, L., and K. B. Katsaros, 1985: Atmospheric water distribution in a midlatitude cyclone observed by the Seasat Scanning Multichannel Microwave Radiometer. *Mon. Wea. Rev.,* **113,** 584–598.

——, and C. Mass, 2004: Major numerical forecast failures over the northeast Pacific. *Wea. Forecasting,* **19,** 338–356.

Miller, D., and K. Katsaros, 1992: Satellite-derived surface latent heat fluxes in a rapidly intensifying marine cyclone. *Mon. Wea. Rev.,* **120,** 1093–1107.

——, and G. Petty, 1998: Moisture patterns in deepening maritime extratropical cyclones. Part I: Correlation between precipitation and intensification. *Mon. Wea. Rev.,* **126,** 2352–2368.

Paciorek, C. J., J. S. Risbey, V. Ventura, and R. D. Rosen, 2002: Multiple indices of Northern Hemisphere cyclone activity, winters 1949–1999. *J. Climate,* **15,** 1573–1590.

Parker, D., 1998: Secondary frontal waves in the North Atlantic region: A dynamical perspective of current ideas. *Quart. J. Roy. Meteor. Soc.,* **124,** 829–856.

Petty, G., and D. Miller, 1995: Satellite microwave observations of precipitation correlated with intensification rate in extratropical oceanic cyclones. *Mon. Wea. Rev.,* **123,** 1904–1911.

Ralph, F., P. Neiman, and G. Wick, 2004: Satellite and CALJET aircraft observations of atmospheric rivers over the eastern North Pacific Ocean during the winter of 1997/98. *Mon. Wea. Rev.,* **132,** 1721–1745.

Randel, D., T. Greenwald, T. von der Haar, G. Stephens, M. Ringerud, and C. Combs, 1996: A new global water vapor database. *Bull. Amer. Meteor. Soc.,* **77,** 1233–1246.

Roebber, P. J., 1984: Statistical analysis and updated climatology of explosive cyclones. *Mon. Wea. Rev.,* **112,** 1577–1589.

Sanders, F., and J. Gyakum, 1980: The synoptic–dynamic climatology of the bomb. *Mon. Wea. Rev.,* **108,** 1589–1606.

Schmidt, G. A., and Coauthors, 2006: Present-day atmospheric simulations using GISS ModelE: Comparison to in situ, satellite, and reanalysis data. *J. Climate,* **19,** 153–192.

Simmons, A. J., and J. K. Gibson, 2000: The ERA-40 project plan. ERA-40 Project Rep. Series 1, European Centre for Medium-Range Weather Forecasts, Reading, United Kingdom, 63 pp.

Simpson, J. J., J. S. Berg, C. J. Koblinsky, G. L. Hufford, and B. Beckley, 2001: The NVAP global water vapor data set: Independent cross-comparison and multiyear variability. *Remote Sens. Environ.,* **76,** 112–129.

Sinclair, M., 1994: An objective cyclone climatology for the Southern Hemisphere. *Mon. Wea. Rev.,* **122,** 2239–2256.

——, 1997: Objective identification of cyclones and their circulation intensity and climatology. *Wea. Forecasting,* **12,** 591–608.

——, and M. Revell, 2000: Classification and composite diagnosis of extratropical cyclogenesis in the southwest Pacific. *Mon. Wea. Rev.,* **128,** 1089–1105.

Soden, B. J., and F. P. Bretherton, 1993: Upper tropospheric relative humidity from the GOES 6.7 μm channel: Method and climatology for July 1987. *J. Geophys. Res.,* **98,** 16 669–16 688.

Starr, D. O'C., and D. P. Wylie, 1990: The 27–28 October 1986 FIRE cirrus case study: Meteorology and clouds. *Mon. Wea. Rev.,* **118,** 2259–2287.

Stohl, A., 2001: A one-year Lagrangian "climatology" of airstreams in the Northern Hemisphere troposphere and lowermost stratosphere. *J. Geophys. Res.,* **106,** 7263–7279.

Tselioudis, G., and C. Jakob, 2002: Evaluation of midlatitude cloud properties in a weather and a climate model: Dependence on dynamic regime and spatial resolution. *J. Geophys. Res.,* **107,** 4781, doi:10.1029/2002JD002259.

Wallace, J. M., G. H. Lim, and M. L. Blackmon, 1988: Relationship between cyclone tracks, anticyclone tracks, and baroclinic waveguides. *J. Atmos. Sci.,* **45,** 439–462.

Wang, H., and R. Fu, 2000a: Influences of ENSO SST anomalies and winter storm tracks on the interannual variability of upper-troposphere water vapor over the Northern Hemisphere extratropics. *J. Climate,* **13,** 59–73.

——, and ——, 2000b: Winter monthly mean atmospheric anomalies over the North Pacific and North America associated with El Niño SSTs. *J. Climate,* **13,** 3435–3447.

Xie, S. C., R. T. Cederwall, and M. Zhang, 2004: Developing long-term single-column model/cloud system-resolving model forcing data using numerical weather prediction products constrained by surface and top of the atmosphere observations. *J. Geophys. Res.,* **109,** D01104, doi:10.1029/2003JD004045.

Yang, S., K.-M. Lau, and K.-M. Kim, 2002: Variations of the east Asian jet stream and Asian–Pacific–American winter climate anomalies. *J. Climate,* **15,** 306–325.

Zhang, M. H., and Coauthors, 2005: Comparing clouds and their seasonal variations in 10 atmospheric general circulation models with satellite measurements. *J. Geophys. Res.,* **110,** D15S02, doi:10.1029/2004JD005021.

Zhang, Y., and W.-C. Wang, 1997: Model-simulated northern winter cyclone and anticyclone activity under a greenhouse warming scenario. *J. Climate,* **10,** 1616–1634.

Zhu, Y., and R. Newell, 1998: A proposed algorithm for moisture fluxes from atmospheric rivers. *Mon. Wea. Rev.,* **126,** 725–735.

Zielinski, G., 2002: A classification scheme for winter storms in the eastern and central United States with an emphasis on nor'easters. *Bull. Amer. Meteor. Soc.,* **83,** 37–51.